



Effects of magnetic–vortical interactions on magnetic splitting

Linlin Kang^{1,4} , Yanru Wang², Zhongzheng Jiang², Jinhua Hao³ ,
Shiying Xiong² , Dixia Fan⁴  and Weicheng Cui⁴

¹Hangzhou International Innovation Institute, Beihang University, Hangzhou, Zhejiang 311115, PR China

²Department of Engineering Mechanics, School of Aeronautics and Astronautics, Zhejiang University, Hangzhou, Zhejiang 310027, PR China

³Kuaishou Technology, Beijing 100085, PR China

⁴Key Laboratory of Coastal Environment and Resources of Zhejiang Province, School of Engineering, Westlake University, Hangzhou, Zhejiang 310030, PR China

Corresponding author: Shiying Xiong, shiying.xiong@zju.edu.cn

(Received 1 September 2024; revised 2 March 2025; accepted 3 March 2025)

We propose an analytical approach based on the Frenet–Serret (FL) frame field, where an FL frame and the corresponding curvature and torsion are defined at each point along magnetic field lines, to investigate the evolution of magnetic tubes and their interaction with vortex tubes in magnetohydrodynamics. Within this framework, simplified expressions for the Lorentz force, its curl, the dynamics of flux tubes and helicity are derived. We further perform direct numerical simulations on the linkage between the magnetic and vortex tubes and investigate the effect of the initial angle θ , ranging from 0° to 45° , on their evolution. Our results show that magnetic tubes with non-zero curvature generate Lorentz forces, which in turn produce dipole vortices. These dipole vortices lead to the splitting of the magnetic tubes into smaller structures, releasing magnetic energy. Both magnetic and vortex tubes exhibit quasi-Lagrangian behaviour, maintaining similar shapes during initial evolution and consistent relative positions over time. A vortex tube with strength comparable to that of the magnetic tube, where the kinetic energy induced by the vortex tube is of the same order as the magnetic energy in the magnetic tube, can inhibit magnetic tube splitting by disrupting the formation of vortex dipoles. Additionally, minor variations in the angular configuration of the vortex tubes significantly influence their interaction with the magnetic field and the evolution of large-scale flow structures.

Key words: magnetic fluids, vortex dynamics, topological fluid dynamics

1. Introduction

Magnetohydrodynamics (MHD) serves as a methodological framework for analysing and characterising the various properties of plasma (Kulsrud 1983; Makwana & Yan 2020; Hoelzl *et al.* 2021). In MHD, the magnetic flux tube represents a region of concentrated magnetic field lines confined within a distinct spatial boundary (Roberts & Webb 1978; Davidson 2017; Toriumi & Hotta 2019). The examination of these flux tubes is crucial for understanding magnetic field behaviour across various domains, including astrophysics (Zhugzhda 2000; Yuan *et al.* 2019), engineering (Stuikys & Sykulski 2018; Tang *et al.* 2018) and space exploration (Levchenko *et al.* 2020; Bowers *et al.* 2021). Moreover, magnetic flux tubes are essential for confining charged particles, such as electrons and ions (Egedal *et al.* 2013; Porto *et al.* 2023), with implications for plasma dynamics in fusion research (You *et al.* 2005; Effenberg *et al.* 2017) and solar physics (Fan 2008; Inoue *et al.* 2018; Manek & Brummell 2021).

Magnetic flux tubes often give rise to complex topological structures such as knots or links, as demonstrated by various studies (see Linton *et al.* 2001; Ricca & Maggioni 2014; Hao & Yang 2021; Zhao & Scalo 2021). These structures are widely recognised as being part of the solar active zone (Lozitsky *et al.* 2000; Chelpanov *et al.* 2015; MacTaggart *et al.* 2021). Beckers & Schröter (1968) investigated the structures of strong magnetic fields, revealing that sunspot active regions can generate numerous magnetic knots. Further exploration of the interactions between ascending flux tubes and magnetic knots on the solar surface was provided by Parker (1978), offering insights into the dynamic process of mutual attraction among magnetic knots within sunspot regions.

The evolution of magnetic flux tubes involves topological transformations, including the breaking, rearrangement and reconnection of magnetic field lines (Ricca 1997; Yamada *et al.* 2010; Özdemir 2021). When magnetic field lines become intertwined, they self-organise into new magnetic configurations, driven by magnetic energy within the plasma (Yin *et al.* 2008). This process often generates intense small-scale structures and facilitates the conversion of magnetic energy near line intersections (Mininni *et al.* 2006). For instance, in Earth's magnetosphere, magnetic reconnection enables interactions between the planet's magnetic field and the solar wind, leading to phenomena such as geomagnetic storms (Gonzalez *et al.* 1994; Angelopoulos *et al.* 2020). Additionally, theoretical insights into the topology of magnetic flux tubes have practical implications for tokamak reactor design (Freidberg *et al.* 2015) and the development of magnetic energy facilities (Domínguez-Lozoya *et al.* 2021).

We utilise the resistive model as an approximation to capture certain effects of localised turbulence (Biskamp 1994). However, resistivity alone is insufficient to fully describe turbulence effects in astrophysical systems such as the Sun, where external noise, instabilities and nonlinear interactions influence reconnection dynamics (Somov & Kosugi 1997; Ren *et al.* 2005; Zweibel & Yamada 2009). While zero resistivity recovers the ideal MHD equations, these equations fail to hold even for an infinitesimal resistivity. Fast reconnection, observed in both laboratory and solar environments, occurs when topological changes outpace resistive rates due to turbulence disrupting the frozen-flux condition (Lazarian & Vishniac 1999; Ji *et al.* 2022), as even in the absence of noise, a sharp current sheet becomes unstable and spontaneously generates turbulence, driving rapid reconnection (Singh *et al.* 2006). Nevertheless, the resistive model offers a practical approximation for certain aspects of magnetic field dynamics, particularly in modelling geometric and topological changes such as tube splitting, where it provides a reasonable description of relevant phenomena (Cassak *et al.* 2005).

We investigate the generation, evolution and energy release associated with the splitting of magnetic flux tubes – a process wherein a single magnetic tube divides into two or

more narrower tubes under specific conditions (Spruit & Roberts 1983). Although the role of magnetic splitting in magnetic energy relaxation has been acknowledged in numerous astronomical observations, quantitative studies of this phenomenon have only recently emerged (see Dumin & Somov 2019; Xiong & Yang 2020a). Dumin & Somov (2020) examined the topological instability behind magnetic splitting using the Gorbachev–Kel’ner–Somov–Shvarts model, revealing that the splitting pattern is driven by the sudden bifurcation-induced emergence of an additional null point. Another analytical approach was developed by Xiong & Yang (2019a, 2020a) to construct flux tubes, which was subsequently applied to the study of magnetic splitting. In Xiong & Yang (2020a), the division of magnetic flux tubes is attributed to the Lorentz force, with this effect diminishing as the twist increases. However, a comprehensive theory that fully explains the underlying mechanisms of this phenomenon remains elusive.

We also highlight the influence of vortices on the evolution of magnetic fields (Berciu *et al.* 2005). In the initial stages of evolution, untwisted magnetic tubes generally create a mutually repulsive flow field due to Lorentz forces (Spicer 1982), leading to ongoing splitting of the magnetic tubes and the formation of geometrically filamentary structures commonly linked with magnetic helicity (Ricca 2013). This behaviour resembles the geometric cascade observed in the helical vortex model (Lundgren 1982, 1993; Xiong & Yang 2019b). However, vortices can disrupt the local flow field, thereby hindering the relaxation of tightly constrained tubular structures into more dispersed floral configurations (Goossens *et al.* 1995; Xiong & Yang 2020b).

This study employs direct numerical simulation (DNS) to investigate the dynamics of magnetic tube evolution and the impact of vortices on MHD flows through their interaction with magnetic fields. In the absence of vortex effects, magnetic tubes typically undergo a topological splitting process as described by Dumin & Somov (2020). We study the Lorentz forces within a Frenet–Serret (FS) frame field along magnetic field lines, aiming to identify the primary factors influencing magnetic tube splitting. Owing to the quasi-Lagrangian nature of magnetic and vortex tubes during their evolution, the motion of vortex tubes initially aligns with that of magnetic tubes, resulting in a stable interaction over time. Furthermore, the evolution of helicity demonstrates that magnetic helicity and cross-helicity are conserved in the absence of viscosity, indicating an approximate topological locking between magnetic and vortex lines.

When vortex tubes with relatively high vorticity strength intersect magnetic tubes at a small angle, the proximity enables the vorticity to affect the splitting process by destabilising the vortex dipoles induced by the Lorentz forces. This effect is also evident in the evolution of magnetic energy, which can be divided into stretching and dissipation components. The presence of vortex tubes typically promotes the elongation and redistribution of magnetic field structures, inhibiting magnetic reconnection and consequently reducing the release of magnetic energy. In contrast, the absence of vortex tubes leads to increased magnetic energy release through the stretching term, promoting magnetic tube splitting. Additionally, we investigate the impact of the angle between vortex tubes and magnetic tubes on dynamic evolution. Our findings show that smaller angles hinder the release of magnetic and kinetic energy, while larger angles facilitate magnetic energy release, aiding in the relaxation of the magnetic field.

We observe that the evolution of magnetic tubes, driven by Lorentz forces, leads to the formation of vortex tubes that nearly coincide with the magnetic structures, thereby naturally motivating our configuration for studying magnetic–vortex interactions in physical systems. The set-up, inspired by recent observations of vortex motions in the solar atmosphere by Tziotziou *et al.* (2023), initialises the system with closely co-located magnetic and vortex tubes. Although idealised, this configuration captures

essential features of real-world magnetic–vortex interactions, establishing a foundation for future investigations into the mutual influence of magnetic and vortex tubes under varying conditions and advancing the understanding of more complex MHD flows.

The paper is organised as follows. Section 2 presents the governing equations for MHD flows and describes the numerical simulation using pseudo-spectral methods, including the configuration of our case studies. Section 3 analyses the morphology and dynamics of magnetic and vortical structures in the flow, aiming to elucidate the mechanisms of magnetic tube splitting through the FS frame field and the role of quasi-Lagrangian dynamics in maintaining stability. In § 4, we discuss the influence of vortex dynamics on the evolution of MHD flows, emphasising the sensitivity of tubular structures to dynamic variations. Section 5 concludes with a summary of the findings and recommendations for future research.

2. Direct numerical simulation of MHD

2.1. Numerical methods

We solve the MHD equations (see Priest & Forbes 2000) as follows:

$$\begin{cases} \frac{\partial \mathbf{u}}{\partial t} + \mathbf{u} \cdot \nabla \mathbf{u} = -\frac{1}{\rho} \nabla p + \frac{1}{\rho} \mathbf{F}_L + \nu_k \nabla^2 \mathbf{u}, & \nabla \cdot \mathbf{u} = 0, \\ \frac{\partial \mathbf{b}}{\partial t} = \nabla \times (\mathbf{u} \times \mathbf{b}) + \nu_m \nabla^2 \mathbf{b}, & \nabla \cdot \mathbf{b} = 0. \end{cases} \quad (2.1)$$

In this system, \mathbf{u} , \mathbf{b} , p , ρ , t , ν_k and ν_m represent the velocity, magnetic induction, pressure, mass density, time, kinematic viscosity and magnetic diffusivity, respectively. The magnetic induction \mathbf{b} is referred to as the magnetic field in this study, although strictly speaking, the magnetic field in vacuum is given by $\mathbf{H} = \mathbf{b}/\mu_0$, where μ_0 denotes the magnetic permeability of free space with a value of $4\pi \times 10^{-7} \text{ H m}^{-1}$. The Lorentz force, \mathbf{F}_L , is given by

$$\mathbf{F}_L \equiv \mathbf{j} \times \mathbf{b}, \quad (2.2)$$

where \mathbf{j} is the current density, related to the magnetic induction \mathbf{b} through Ampère’s law: $\mathbf{j} = \nabla \times \mathbf{b}/\mu_0$. The fluid is assumed to be incompressible, with a constant density ρ . We set $\nu_k = \nu_m$, which results in a magnetic Prandtl number, Pr_m , of unity, defined as the ratio of kinematic viscosity to magnetic diffusivity (Hasimoto 1959). This choice simplifies the MHD system, facilitating both mathematical analysis and numerical simulations, particularly in qualitative studies (Linton *et al.* 2001; Kivotides 2018).

We adopt the dimensionless form of (2.1), maintaining the original form of the variables for simplicity. We perform numerical simulations of MHD flows within a periodic cube Ω of side length $L = 2\pi$. The governing equation (2.1) is symmetrically reformulated using the variables $\mathbf{z}^\pm = \mathbf{u} \pm \mathbf{b}$, as introduced by Elsasser (1950). These equations are solved with a pseudo-spectral method, following the approach of Aluie (2009), which provides highly accurate computation of spatial derivatives through Fourier transformations. To reduce aliasing errors, we use the two-thirds truncation method, with a maximum wavenumber $k_{max} \approx N/3$. Time integration of the Fourier coefficients is carried out using a second-order Runge–Kutta scheme, with the time step chosen to maintain the Courant–Friedrichs–Lewy number below 0.5 for numerical stability. The accuracy of our MHD solver has been validated in previous studies, as cited in Hao *et al.* (2019), Xiong & Yang (2020*a*) and Hao & Yang (2021). Details of grid convergence testing are provided in Appendix A.

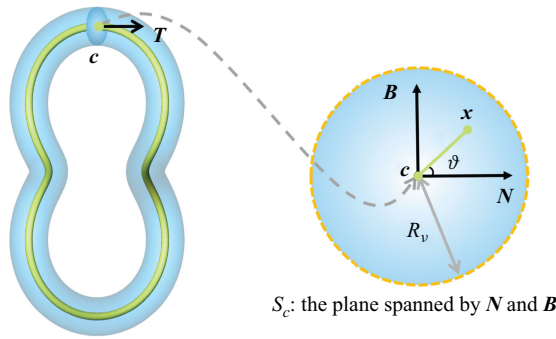


Figure 1. Schematic diagram showing the relationship between the intrinsic coordinates (s, ϱ, ϑ) and the Cartesian coordinates (x, y, z) . The flux tube is outlined in light blue, with its central axis indicated in yellow-green. The cross-sectional view of the flux tube is enclosed by an orange dashed line.

We investigate the interaction between magnetic and vortical flux tubes using the methodology of Xiong & Yang (2019a, 2020a). The initial conditions include tubular structures derived from a continuous, differentiable curve $C : \mathbf{x} = \mathbf{c}(s)$ in three-dimensional space \mathbb{R}^3 , parametrised by arc length $s \in [0, L_C]$, where L_C is the length of the curve. In figure 1, the spatial coordinates $\mathbf{x} = (x, y, z)$ are expressed in the FS frame as $\mathbf{x} = \mathbf{c}(s) + \varrho \cos \vartheta \mathbf{N} + \varrho \sin \vartheta \mathbf{B}$, where $\mathbf{T} \equiv d\mathbf{c}/ds$ is the unit tangent vector, $\mathbf{N} \equiv (d\mathbf{T}/ds)/(|d\mathbf{T}/ds|)$ is the unit normal vector and $\mathbf{B} \equiv \mathbf{T} \times \mathbf{N}$ is the unit binormal vector. Here, $\varrho = |\mathbf{x} - \mathbf{c}|$ denotes the distance between $\mathbf{c}(s)$ and \mathbf{x} , and $\vartheta \in [0, 2\pi)$ is the angle in the plane defined by \mathbf{N} and \mathbf{B} from the unit normal vector to \mathbf{x} . This configuration positions curve C as the central axis of the flux tube.

In the coordinate system (s, ϱ, ϑ) , the flux tube formulation is given by (Xiong & Yang 2019a)

$$\mathbf{v}(s, \varrho, \vartheta) = f(\varrho)\mathbf{T}, \tag{2.3}$$

where the kernel function is $f(\varrho) = \exp[-\varrho^2/(2\sigma^2)]/(2\pi\sigma^2)$ with $\sigma = 1/(16\sqrt{2\pi}) \approx 0.025$. The flux tube's estimated radius R_v is approximately 5σ , encompassing over 99.999% of the toroidal flux. We restrict \mathbf{v} within R_v , ensuring no self-intersections as long as R_v is smaller than the minimum curvature radius of the central axis C .

We express the initial magnetic field \mathbf{b} in (2.1) using (2.3) as $\mathbf{b} = \Gamma_m \mathbf{v}$, where Γ_m denotes the circulation of the initial magnetic tube. Similarly, the vorticity field is given by $\boldsymbol{\omega} = \Gamma_k \mathbf{v}$, with Γ_k representing the circulation of the initial vortex tube. To obtain the velocity field \mathbf{u} in (2.1), we solve $\boldsymbol{\omega} = \nabla \times \mathbf{u}$ and $\nabla \cdot \mathbf{u} = 0$ using the Fourier transform: $\mathbf{u} = \mathcal{F}^{-1}(i\mathbf{k} \times \hat{\boldsymbol{\omega}}/|\mathbf{k}|^2)$, where \mathcal{F}^{-1} denotes the inverse Fourier transform, \mathbf{k} is the wavenumber vector and $\hat{\boldsymbol{\omega}} = \mathcal{F}(\boldsymbol{\omega})$ is the Fourier transform of the vorticity field.

2.2. Initial configurations

We generate the initial flux tubes as a pair of interconnected tubes. The parametric equation $\mathbf{c}(\zeta) = [c_x(\zeta), c_y(\zeta), c_z(\zeta)]$ defines the axis of the first flux tube:

$$\begin{cases} c_x(\zeta) = \pi + [1 + 0.5 \cos(2\zeta)] \cos(\zeta), \\ c_y(\zeta) = \pi + [1 + 0.5 \cos(2\zeta)] \sin(\zeta), \\ c_z(\zeta) = \pi - 1.5 - 0.5 \sin(2\zeta). \end{cases} \tag{2.4}$$

The axis of the second flux tube is obtained by rotating the curve from (2.4) clockwise by $\pi/2$ around the line at $(x, y) = (\pi, \pi)$. As a result, the initial configuration comprises

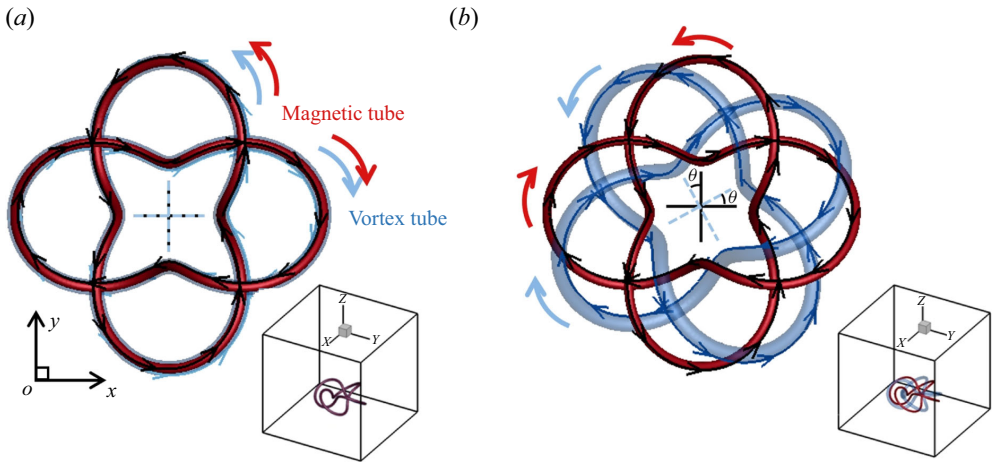


Figure 2. Isosurfaces of $|\mathbf{b}|$ and $|\boldsymbol{\omega}|$ for (a) $L_m L_k$ with $\theta = 0^\circ$ and (b) $L_m L_k$ with $\theta = 30^\circ$.

two interconnected tubes, leading to scenarios where the magnetic and vortex tubes may exhibit either right- or left-handed linkages. For simplicity, the arc length parameter for curve C is not used in the above equation. Detailed formulas for computing the geometric properties of curves using a generalised parameter format are provided in Appendix A of Xiong & Yang (2020a).

We investigate various magnetic–vortex configurations, considering the presence or absence of initial vorticity and magnetic fields. Specifically, we examine systems with initial left-handed linkage ($L_m L_k$) and right-handed linkage ($R_m R_k$) for magnetic and vortex tubes, as well as pure initial magnetic flow ($L_m O_k, R_m O_k$) and purely vortical flow ($O_m L_k, O_m R_k$), resulting in four distinct reference categories. A right-handed linkage indicates that the two interconnected closed flux tubes share the same orientation, whereas a left-handed linkage implies that they have opposite orientations. While left-handed and right-handed linkages provide a useful classification, the key determinant of their dynamics in MHD flows lies in the relative spatial arrangement and interaction of the tubes, particularly in relation to the alignment of the currents and the reconnection behaviour. We also investigate how the initial angle between the magnetic and vortex tubes influences flux tube evolution. In our notation, ‘R’ and ‘L’ represent flux tubes with right-handed (positive linking number +2) and left-handed linkages (negative linking number –2), respectively, while ‘O’ indicates the absence of corresponding flux tubes. The subscripts ‘m’ and ‘k’ denote magnetic and kinematic vortex tubes, with ‘ θ ’ specifying their relative angle.

Figure 2 shows isosurfaces of $|\boldsymbol{\omega}|$ and $|\mathbf{b}|$ for various flux tube configurations, highlighting their coherent and concentrated structures. This confirms the appropriateness of the constructed flux links as initial conditions for DNS. Due to the short time scales considered, the flow structure remains approximately centred within the computational domain. The effect of periodic boundaries on the flow is minimal, given the distance-squared decay of the velocity field as described by the Biot–Savart law.

Table 1 provides the parameters and statistics for representative initial flux tubes, including the grid size N , which determines the simulation resolution. It also lists several dimensionless parameters, including the kinetic Reynolds number $Re_k = \Gamma_k / \nu_k$, which characterises the relative dominance of inertial forces over viscous dissipation in the kinetic field, and the magnetic Reynolds number $Re_m = Re_k \cdot Pr_m$, which quantifies the relative importance of inertial versus diffusive effects in the magnetic

Case	θ	N	Re_k	Re_m	E_k	E_m	ϵ_k	ϵ_m	H_c	H_m
$L_m L_k$	0°	512	861.4	861.4	5.0	5.0	55.29	332.03	-12.90	-3.08
	0°	512	1722.8	1722.8	5.0	5.0	27.65	161.02	-12.90	-3.08
	0°	1024	3445.6	3445.6	5.0	5.0	13.82	80.48	-12.90	-3.08
	0°	1024	6891.2	6891.2	5.0	5.0	6.91	40.24	-12.90	-3.08
	2°	512	1722.8	1722.8	5.0	5.0	27.65	161.02	-10.42	-3.08
	4°	512	1722.8	1722.8	5.0	5.0	27.65	161.02	-5.71	-3.08
	7.5°	512	1722.8	1722.8	5.0	5.0	27.65	161.02	-1.14	-3.08
	15°	512	1722.8	1722.8	5.0	5.0	27.65	161.02	-0.009	-3.08
$R_m R_k$	0°	512	1722.8	1722.8	5.0	5.0	22.76	161.02	20.84	5.51
$L_m O_k$	-	512	0.0	0.0	0.0	5.0	0.0	332.03	0.0	-3.08
	-	512	0.0	0.0	0.0	5.0	0.0	161.02	0.0	-3.08
	-	1024	0.0	0.0	0.0	5.0	0.0	80.48	0.0	-3.08
	-	1024	0.0	0.0	0.0	5.0	0.0	40.24	0.0	-3.08
$R_m O_k$	-	512	0.0	0.0	0.0	5.0	0.0	161.02	0.0	5.51
$O_m L_k$	-	512	1722.0	--	5.0	0.0	27.65	0.00	0.00	0.00
$O_m R_k$	-	512	1722.0	--	5.0	0.0	22.76	0.00	0.00	0.00

Table 1. Parameters and statistics for the initial configurations of selected simulations. Here R and L denote right-handed and left-handed flux tubes with linking numbers $+2$ and -2 , respectively. Subscripts m and k refer to magnetic and kinematic vortex tubes, with θ specifying their angle. The initial fluxes are set to $\Gamma_k = 17.228$ and $\Gamma_m = 1.036$, ensuring equal initial magnetic and kinetic energy in simulations with both types of tubes.

field. Additionally, the table provides the kinetic energy $E_k = \sum_k |\hat{\mathbf{u}}(\mathbf{k})|^2/2$ and magnetic energy $E_m = \sum_k |\hat{\mathbf{b}}(\mathbf{k})|^2/2$, calculated by using Fourier coefficients $\hat{\mathbf{b}} = \mathcal{F}(\mathbf{b})$ and $\hat{\mathbf{u}} = \mathcal{F}(\mathbf{u})$. Additionally, it includes the kinetic dissipation rate $\epsilon_k = \nu_k \sum_k (|\mathbf{k}| |\hat{\mathbf{u}}(\mathbf{k})|)^2$ and magnetic dissipation rate $\epsilon_m = \nu_m \sum_k (|\mathbf{k}| |\hat{\mathbf{b}}(\mathbf{k})|)^2$, which quantify the efficiency of the energy dissipation mechanisms in the fluid and magnetic fields. Helicity statistics are also provided, including cross-helicity $H_c = \int_\Omega \mathbf{u} \cdot \mathbf{b} \, d\Omega$ and magnetic helicity $H_m = \int_\Omega \mathbf{a} \cdot \mathbf{b} \, d\Omega$, where $\mathbf{a} = \mathcal{F}^{-1}(i\mathbf{k} \times \hat{\mathbf{b}}/|\mathbf{k}|^2)$. Cross-helicity measures the correlation between the velocity and magnetic fields, while magnetic helicity provides insight into the twist and linkage of the magnetic field lines. For cases with vortex tubes, the initial vorticity flux, Γ_k , is set to 17.228, while for cases with magnetic tubes, the initial magnetic flux, Γ_m , is set to 1.036. This ensures that in simulations with both a magnetic tube and a vortex tube, the initial magnetic energy of the magnetic tube equals the initial kinetic energy of the vortex tube.

We investigate the evolution of magnetic tubes and their interactions with vortex tubes. As shown in figure 3, a phenomenon observed is the splitting of magnetic tubes during their evolution. This study systematically explores this process by integrating theoretical analysis of the governing equations with a quantitative assessment of numerical results. Specifically, vortex dynamics analysis is used to clarify the role of vortex tubes in magnetic tube splitting.

Additionally, we observe that, in our numerical simulations involving both magnetic and vortex tubes, the Lorentz force is substantially larger than the inertial force. This relationship can be characterised by the interaction parameter $N_I = \Gamma_m^2 / [\rho \mu_0 Re_k \nu_k \nu_m (R_v)^2] = (\Gamma_m^2 Re_k) / \rho \mu_0 (\Gamma_k R_v)^2$, which quantifies the balance between

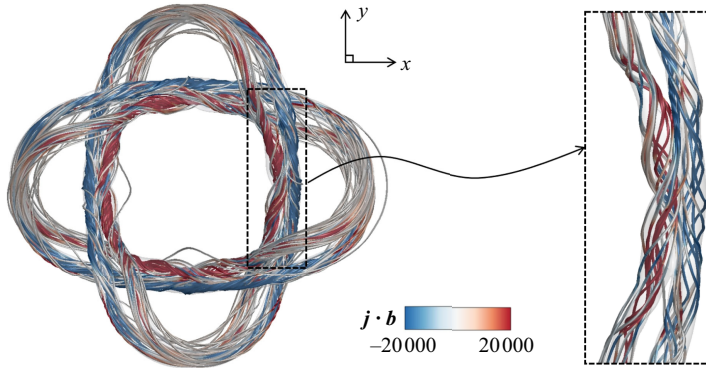


Figure 3. Splitting of the magnetic tube for case $L_m O_k$ with $Re_m = 414.4$ at $t = 0.0175$. Integral curves of \mathbf{b} are coloured by the scalar field $\mathbf{j} \cdot \mathbf{b}$. The right-hand subfigure provides a zoomed view of the dashed box area from the left-hand subfigure.

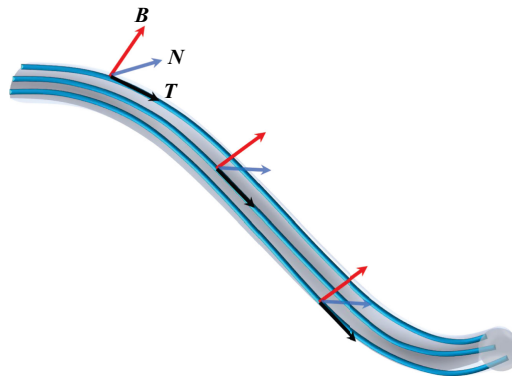


Figure 4. Frenet–Serret frames generated by magnetic field lines. The unit tangent, normal and binormal vectors are represented by black, blue and red arrows, respectively.

Lorentz and inertial forces in the system (Kivotides 2018, 2019). In the simulations presented herein, $N_I \gg 1$, and in this regime, the morphologies of the vorticity and magnetic field structures exhibit notable similarity. This phenomenon is further explored in the following sections and aligns with the observations of Kivotides (2018).

3. Magnetohydrodynamic flows in the FS frame field

3.1. The FS frame fields

To facilitate the analysis of dynamic flow fields, we extend the FS frame throughout the flux tube domain. This FS frame is defined where the magnetic field and the curvature of the magnetic lines are both non-zero, although it is important to note that inflexion points may exist in realistic scenarios. Specifically, we define a FS coordinate system at each point along the magnetic field lines, establishing a unit frame field $[\mathbf{T}(\mathbf{x}), \mathbf{N}(\mathbf{x}), \mathbf{B}(\mathbf{x})]$ at locations where the magnetic field is non-zero, as depicted in figure 4. At each point \mathbf{c} along these magnetic lines, the vectors $[\mathbf{T}(\mathbf{c}), \mathbf{N}(\mathbf{c}), \mathbf{B}(\mathbf{c})]$ follow the FS formulas:

$$\mathbf{T} \cdot \nabla \mathbf{T} = \kappa \mathbf{N}, \quad \mathbf{T} \cdot \nabla \mathbf{N} = -\kappa \mathbf{T} + \tau \mathbf{B}, \quad \mathbf{T} \cdot \nabla \mathbf{B} = -\tau \mathbf{N}. \quad (3.1)$$

Here, κ and τ represent the curvature and torsion of the curve, respectively.

Let T , N and B be column vectors that form an orthogonal matrix $\mathcal{O} = [T, N, B]$. Utilising the properties of the matrix trace, for any matrix A , we have

$$\text{Tr}(A) = \text{Tr}(\mathcal{O}^{-1}A\mathcal{O}) = \text{Tr}(\mathcal{O}^T A\mathcal{O}) = T^T AT + N^T AN + B^T AB. \quad (3.2)$$

Since T , N and B are unit vectors, and applying (3.2) and $\nabla \cdot A = \text{Tr}(\nabla A)$, we obtain

$$\begin{cases} \nabla \cdot T = T \cdot \nabla T \cdot T + N \cdot \nabla T \cdot N + B \cdot \nabla T \cdot B = N \cdot \nabla T \cdot N + B \cdot \nabla T \cdot B, \\ \nabla \cdot N = T \cdot \nabla N \cdot T + N \cdot \nabla N \cdot N + B \cdot \nabla N \cdot B = T \cdot \nabla N \cdot T + B \cdot \nabla N \cdot B, \\ \nabla \cdot B = T \cdot \nabla B \cdot T + N \cdot \nabla B \cdot N + B \cdot \nabla B \cdot B = T \cdot \nabla B \cdot T + N \cdot \nabla B \cdot N. \end{cases} \quad (3.3)$$

Additionally, for three-dimensional vectors f and g , using

$$\nabla \times (f \times g) = -(\nabla \cdot f)g + (\nabla \cdot g)f + g \cdot \nabla f - f \cdot \nabla g \quad (3.4)$$

and (3.3), we obtain

$$\begin{aligned} \nabla \times T &= \nabla \times (N \times B) = -(\nabla \cdot N)B + (\nabla \cdot B)N + B \cdot \nabla N - N \cdot \nabla B \\ &= (N \cdot \nabla T \cdot B - B \cdot \nabla T \cdot N)T + (\nabla \cdot B + N \cdot \nabla N \cdot B)N \\ &\quad + (B \cdot \nabla N \cdot B - \nabla \cdot N)B \\ &= (N \cdot \nabla T \cdot B - B \cdot \nabla T \cdot N)T + (T \cdot \nabla B \cdot T)N - (T \cdot \nabla N \cdot T)B. \end{aligned} \quad (3.5)$$

Similarly, we have

$$\begin{cases} \nabla \times N = -(N \cdot \nabla B \cdot N)T + (B \cdot \nabla N \cdot T - T \cdot \nabla N \cdot B)N + (N \cdot \nabla T \cdot N)B, \\ \nabla \times B = (B \cdot \nabla N \cdot B)T - (B \cdot \nabla T \cdot B)N + (T \cdot \nabla B \cdot N - N \cdot \nabla B \cdot T)B. \end{cases} \quad (3.6)$$

Substituting (3.1) into (3.3), (3.5) and (3.6) yields

$$\begin{cases} \nabla \cdot T = N \cdot \nabla T \cdot N + B \cdot \nabla T \cdot B, \\ \nabla \cdot N = -\kappa + B \cdot \nabla N \cdot B, \\ \nabla \cdot B = N \cdot \nabla B \cdot N \end{cases} \quad (3.7)$$

and

$$\begin{cases} \nabla \times T = (N \cdot \nabla T \cdot B - B \cdot \nabla T \cdot N)T + \kappa B, \\ \nabla \times N = -(N \cdot \nabla B \cdot N)T - (\tau + B \cdot \nabla T \cdot N)N + (N \cdot \nabla T \cdot N)B, \\ \nabla \times B = (B \cdot \nabla N \cdot B)T - (B \cdot \nabla T \cdot B)N + (N \cdot \nabla T \cdot B - \tau)B. \end{cases} \quad (3.8)$$

3.2. Lorentz force in the FS frame field

By aligning the FS frame with the magnetic field lines, the tangent vector T is made parallel to the magnetic field. Within this coordinate system, we investigate the Lorentz force acting on the magnetic tube and elucidate the mechanism underlying its splitting.

Using the FS frame field, the Lorentz force, as expressed in (2.2), can be represented as

$$F_L = -\nabla b \cdot b + b \cdot \nabla b = -\frac{1}{2}\nabla b^2 + b(T \cdot \nabla b)T + \kappa b^2 N. \quad (3.9)$$

Here, κ denotes the curvature of the magnetic lines. We remark that (T, B, N) and κ are computed for each magnetic field line considered as a parametrised curve. Consequently, these quantities define fields that are distributed throughout the flux tube. In Ricca (2005), the Lorentz force is derived through the geometry of magnetic field lines, with a focus

on their curvature and torsion. The study emphasises how the curvature of the magnetic field lines contributes to the instability of flux tubes, particularly when inflection points are present. Similarly, (3.9) provides a geometrical interpretation of the forces acting on the flux tubes, highlighting the role of curvature in destabilising the magnetic structures.

Given the divergence-free property of the vector field \mathbf{b} in (2.1), we arrive at the following relation:

$$b\nabla \cdot \mathbf{T} + \mathbf{T} \cdot \nabla b = 0. \tag{3.10}$$

Substituting (3.10) into (3.9) yields

$$\mathbf{F}_L = -\frac{1}{2}\nabla b^2 + b^2 [-(\nabla \cdot \mathbf{T})\mathbf{T} + \kappa N]. \tag{3.11}$$

We focus on the influence of the Lorentz force on vorticity evolution to elucidate the vortex dynamics induced by MHD effects. To evaluate the vorticity evolution, we apply the curl operator to the first equation in (2.1), yielding

$$\frac{D\omega}{Dt} = \omega \cdot \nabla \mathbf{u} + \nu_k \nabla^2 \omega + \nabla \times \mathbf{F}_L. \tag{3.12}$$

Here, $D/Dt = \partial/\partial t + \mathbf{u} \cdot \nabla$ represents the material derivative. This Lagrangian equation describes the dynamics of vorticity during the shearing process. The vorticity generation arises from the curl of the Lorentz force, which is induced by the magnetic field.

Taking the curl of (3.11) yields

$$\nabla \times \mathbf{F}_L = \nabla \times \left\{ b^2 [-(\nabla \cdot \mathbf{T})\mathbf{T} + \kappa N] \right\}. \tag{3.13}$$

Equation (3.13) reveals that the curl of the Lorentz force splits into two components: $\nabla \times \mathbf{F}_L = \boldsymbol{\omega}^g + \boldsymbol{\omega}^b$. The first component, $\boldsymbol{\omega}^g$, is defined as

$$\boldsymbol{\omega}^g = b^2 \nabla \times [-(\nabla \cdot \mathbf{T})\mathbf{T} + \kappa N] \tag{3.14}$$

and is sensitive to the geometric configuration of the magnetic field lines. On the other hand, the second component, $\boldsymbol{\omega}^b$, is given by

$$\boldsymbol{\omega}^b = (\nabla b^2) \times [-(\nabla \cdot \mathbf{T})\mathbf{T} + \kappa N] \tag{3.15}$$

and is sensitive to variations in magnetic intensity.

The splitting of the magnetic tube is noticeable in the early stages of its evolution. During this phase, the Lorentz force is largely influenced by the initial magnetic field configuration. Accordingly, we examine the initial condition described by (2.3), where the helicity of the vector field is influenced by the writhe of the tube axis (Xiong & Yang 2019a). At this stage, the magnetic field lines have a relatively simple structure, which allows for a more straightforward decomposition of the Lorentz force.

Within the flux tube of radius R_v , the flux lines corresponding to (2.3) are parallel, thus satisfying

$$\mathbf{N} \cdot \nabla \mathbf{T} = \mathbf{B} \cdot \nabla \mathbf{T} = \mathbf{0}. \tag{3.16}$$

Since $\nabla \mathbf{T}$ is a second-order tensor, its contraction with vectors yields a vector. From (3.1) and (3.16), we also derive the following system of equations:

$$\mathbf{B} \cdot \nabla (\mathbf{T} \cdot \nabla \mathbf{T}) = \mathbf{0}, \quad \mathbf{N} \cdot \nabla (\mathbf{T} \cdot \nabla \mathbf{T}) = \kappa^2 \mathbf{N}, \tag{3.17}$$

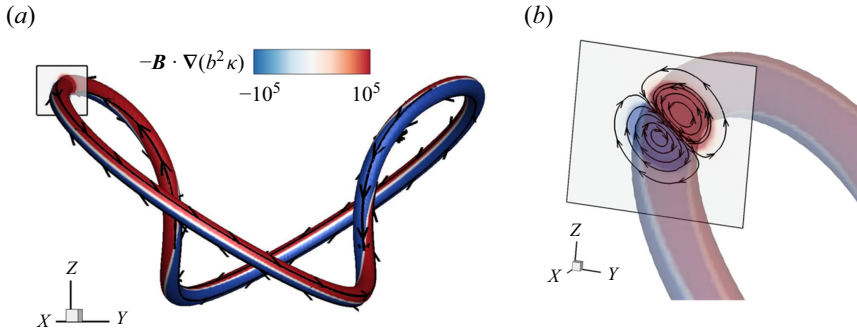


Figure 5. (a) Isosurface of $|b|$ for the initial flux tube from (2.3), colour-coded by $-\mathbf{B} \cdot \nabla(b^2\kappa)$. Black lines are integrals of $-\mathbf{B} \cdot \nabla(b^2\kappa)\mathbf{T}$. (b) Zoomed view of the flux tube near the region marked by the black square in (a), with black lines indicating the integral curves of $\nabla \times (\nabla \times \mathbf{F}_L)$, illustrating the dipole structure induced by the magnetic field.

which leads to

$$\mathbf{B} \cdot \nabla \mathbf{N} \cdot \mathbf{B} = \mathbf{B} \cdot \nabla \left(\frac{\mathbf{T} \cdot \nabla \mathbf{T}}{\kappa} \right) \cdot \mathbf{B} = 0, \quad \mathbf{N} \cdot \nabla \mathbf{B} \cdot \mathbf{N} = -\mathbf{N} \cdot \nabla \left(\frac{\mathbf{T} \cdot \nabla \mathbf{T}}{\kappa} \right) \cdot \mathbf{B} = 0. \tag{3.18}$$

Using (3.16) and (3.18), the expressions represented by (3.7) and (3.8) can be simplified to the following results:

$$\nabla \cdot \mathbf{T} = 0, \quad \nabla \cdot \mathbf{N} = -\kappa, \quad \nabla \cdot \mathbf{B} = 0 \tag{3.19}$$

and

$$\nabla \times \mathbf{T} = \kappa \mathbf{B}, \quad \nabla \times \mathbf{N} = -\tau \mathbf{N}, \quad \nabla \times \mathbf{B} = -\tau \mathbf{B}. \tag{3.20}$$

Here, κ and τ denote the curvature and torsion of the curve, respectively.

We remark that both \mathbf{B} and \mathbf{N} in (3.20) are Beltrami vector fields (see Reed 1995), which can be linked to chaotic magnetic lines in MHD flows (see Smiet *et al.* 2015). The analysis method used for this local frame field is similar to the approach of Gibbon *et al.* (2006) for quaternions, as both involve differentiating the local frame to capture the fluid’s key dynamics.

Using (3.19) and (3.20), we simplify (3.13) to

$$\nabla \times \mathbf{F}_L = \nabla \times (b^2\kappa\mathbf{N}) = - \left[\mathbf{B} \cdot \nabla (b^2\kappa) \right] \mathbf{T} - b^2\kappa\tau\mathbf{N} + b^2(\mathbf{T} \cdot \nabla\kappa)\mathbf{B}. \tag{3.21}$$

In this study, dynamical interactions are observed within the elongated tubular structures where

$$\left| \left[\mathbf{B} \cdot \nabla (b^2\kappa) \right] \mathbf{T} \right| \gg \left| b^2\kappa\tau\mathbf{N} \right| \quad \text{and} \quad \left| \left[\mathbf{B} \cdot \nabla (b^2\kappa) \right] \mathbf{T} \right| \gg \left| b^2(\mathbf{T} \cdot \nabla\kappa)\mathbf{B} \right|. \tag{3.22}$$

This dominance arises due to the typically large gradient of b . Consequently, the first term in (3.21) is the primary contributor to the evolution of the magnetic tube.

Figure 5 shows the distribution of the magnitude of the first term from (3.21) along the initial magnetic tube described by (2.3). The term $[-\mathbf{B} \cdot \nabla(b^2\kappa)]\mathbf{T}$ dominates over the other terms, creating a vortex source along the tube’s axis. Additionally, this term varies in sign along the binormal direction, indicating opposing vortex sources, as illustrated in figures 5(a) and 5(b). The other terms, $|b^2\kappa\tau\mathbf{N}|$ and $|b^2(\mathbf{T} \cdot \nabla\kappa)\mathbf{B}|$, reach their maxima where $\kappa\tau$ and $(\mathbf{T} \cdot \nabla\kappa)$ are largest, respectively. However, these terms are generally much smaller than the first term (figures not shown).

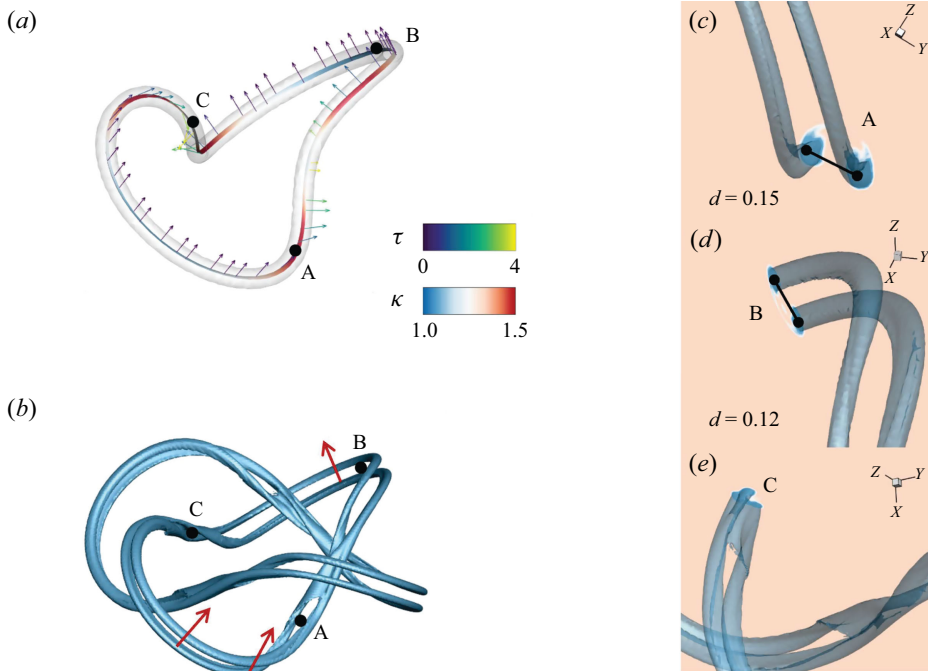


Figure 6. (a) Initial geometry of a single connected magnetic tube in the linked configuration $L_m O_k$. The grey semi-transparent tube shows the isosurface of magnetic field strength, with curvature indicated by the colour-coded centreline. The vectors along the centreline represent the binormal vector B , with their length and colour corresponding to the torsion τ . Positions A, B and C correspond to the locations of maximum curvature, minimum curvature and maximum torsion, respectively. (b) Isosurface of $|b| = 50$ at $t = 0.01$, with red arrows indicating the direction of the binormal vector. Zoomed views of (b) are provided in (c) near A, (d) near B and (e) near C. The distance between the split tubes is denoted by d .

Figure 6(a) shows the initial distributions of curvature κ , torsion τ and binormal vector B along the central line of one of the flux tubes in the $L_m O_k$ case. The variations in curvature and torsion are relatively small. Positions A, B and C correspond to the locations of maximum curvature, minimum curvature and maximum torsion, respectively. Figure 6(b) indicates that the splitting direction is closely aligned with the binormal direction of the initial magnetic tube. At position A, where curvature is greater than that at B, the distance between the split tubes is larger, as shown in figures 6(c) and 6(d). It is observed that greater curvature intensifies the formation of vortex pairs, thereby accelerating the splitting of the tube. Figure 6(e) illustrates that twisting can hinder the magnetic tube's splitting, in agreement with Xiong & Yang (2020b).

We remark that each term in (3.21) involves curvature. For instance, in a one-dimensional cylindrical magnetic tube with a flux distribution described by (2.3), where $\kappa = 0$, the curl of the Lorentz force, $\nabla \times F_L$, equals zero. Consequently, such a cylindrical magnetic tube does not act as a source of vorticity and thus does not lead to the splitting of the magnetic tube.

If the initial magnetic tube possesses curvature, even if it remains constant along the magnetic field lines, tube splitting can still occur. For example, for a magnetic tube with its central line lying in a plane and under the conditions $\tau = 0$ and $T \cdot \nabla \kappa = 0$, the expression of (3.21) simplifies to $\nabla \times F_L = -(\kappa B \cdot \nabla b^2)T$. This indicates that the vorticity source is aligned parallel to the magnetic tube.

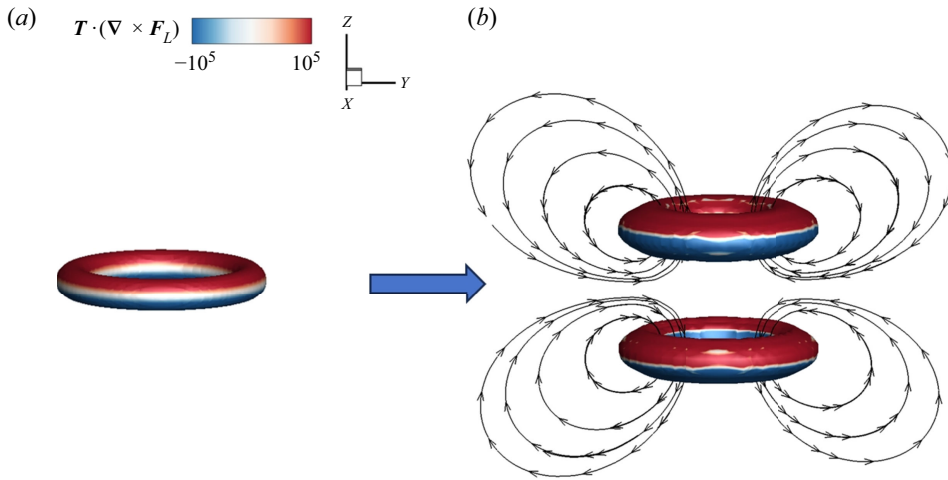


Figure 7. Isosurfaces of $|b|$ for a flow with an initially toroidal magnetic tube of constant curvature $\kappa = 4$ for (a) $|b| = 50$ at $t = 0$ and (b) $|b| = 20$ at $t = 0.005$. The isosurfaces are colour-coded by $T \cdot (\nabla \times F_L)$, with streamlines integrated along u in (b).

Figures 7(a) and 7(b) illustrate the evolution of the $|b|$ isosurface, coloured by $T \cdot (\nabla \times F_L)$, at $t = 0$ and 0.005 . The initial toroidal magnetic tube generates opposing vortex sources in the positive and negative z directions, causing them to move apart. As they separate, the split tubes continue to produce opposing vortex sources, which may lead to sustained tube splitting. In this magnetic tube configuration, we further confirm that a larger curvature κ leads to a greater separation between the split tubes, driven by the stronger vortex pairs induced by $-(\kappa \mathbf{B} \cdot \nabla b^2) \mathbf{T}$.

3.3. Material properties of integral curves in vector fields

A key feature observed during the evolution is that the magnetic and vortex tubes exhibit quasi-Lagrangian characteristics, approximately following the fluid velocity field while interacting with each other. This behaviour leads to the vortex tubes induced by the magnetic field reflecting the motion of the magnetic tubes in the early stages, including similar splitting phenomena. We explore this behaviour through an analysis of the governing equations for the vorticity and magnetic fields.

Specifically, despite the effects of magnetic interactions, the flow field associated with the evolution of strong magnetic tubes closely follows the Helmholtz (1858) vorticity conservation theorem and the Alfvén (1943) frozen-in field theorem. The near-preservation of these conservation laws underscores the robustness of Lagrangian dynamics, even under strong magnetic influences.

To analyse the temporal evolution of the vorticity field, we neglect viscosity and apply the approximation

$$\nabla \times F_L \approx - \left[\mathbf{B} \cdot \nabla (b^2 \kappa) \right] \mathbf{T} \tag{3.23}$$

to (3.21). Consequently, (3.12) simplifies to

$$\frac{D\omega}{Dt} \approx \omega \cdot \nabla \mathbf{u} - \left[\mathbf{B} \cdot \nabla (b^2 \kappa) \right] \mathbf{T}. \tag{3.24}$$

For the temporal evolution of the magnetic field, we consider the second equation in (2.1). By substituting $\nabla \times (\mathbf{u} \times \mathbf{b})$ with $(\mathbf{b} \cdot \nabla \mathbf{u} - \mathbf{u} \cdot \nabla \mathbf{b})$ and neglecting magnetic viscous dissipation, the equation simplifies to

$$\frac{D\mathbf{b}}{Dt} \approx \mathbf{b} \cdot \nabla \mathbf{u}. \tag{3.25}$$

Thus, both the magnetic equation (3.25) and the vorticity equation (3.24) can be approximately reduced to a unified form:

$$\frac{D\mathbf{L}}{Dt} = \mathbf{L} \cdot \nabla \mathbf{u} + \lambda \mathbf{L}, \tag{3.26}$$

where $\lambda = 0$ for $\mathbf{L} = \mathbf{b}$ and $\lambda = -[\mathbf{B} \cdot \nabla(b^2\kappa)]/|\boldsymbol{\omega}|$ for $\mathbf{L} = \boldsymbol{\omega}$. We present Corollary 1, which shows that the integral curves of \mathbf{L} in (3.26) correspond to material curves.

COROLLARY 1. *Assuming the vector field \mathbf{L} satisfies (3.26), the integral curves of \mathbf{L} are material curves.*

Proof. Assume that $\phi(\mathbf{x}, t)$ is a scalar field that evolves over time, with its isosurfaces representing level sets of constant ϕ . Initially, these isosurfaces are aligned with the vector field \mathbf{L} , implying that \mathbf{L} lies tangentially along the isosurfaces, i.e.

$$\mathbf{L} \cdot \nabla \phi|_{t=0} = 0, \tag{3.27}$$

and that the isosurfaces of ϕ are material surfaces, satisfying $D\phi/Dt = 0$, we have

$$\frac{D(\mathbf{L} \cdot \nabla \phi)}{Dt} = \frac{D\mathbf{L}}{Dt} \cdot \nabla \phi + \mathbf{L} \cdot \frac{D(\nabla \phi)}{Dt} = \frac{D\mathbf{L}}{Dt} \cdot \nabla \phi - \mathbf{L} \cdot \nabla \mathbf{u} \cdot \nabla \phi. \tag{3.28}$$

Substituting (3.26) into (3.28), we get

$$\frac{D(\mathbf{L} \cdot \nabla \phi)}{Dt} = \lambda \mathbf{L} \cdot \nabla \phi. \tag{3.29}$$

Combining (3.27) and (3.29), we conclude $\mathbf{L} \cdot \nabla \phi \equiv 0$. This implies that the material surfaces initially parallel to \mathbf{L} remain parallel to \mathbf{L} during the evolution.

Since the integral curves of the vector field \mathbf{L} represent the intersection lines of two independent material surfaces, these curves are material curves themselves. \square

We remark that the material properties of the vector field \mathbf{L} in Corollary 1 can also be interpreted through its Clebsch representation, as detailed in Tao *et al.* (2021), Yang *et al.* (2021) and Xiong *et al.* (2022). Additionally, when $\lambda = 0$ in (3.26), this corollary reduces to the classical Helmholtz (1858) vorticity conservation theorem and the Alfvén (1943) frozen-in field theorem, both describing the conservation of vortex and magnetic surfaces, respectively.

Corollary 1 confirms that both magnetic and vortex tubes in the MHD flow field exhibit similar quasi-Lagrangian properties. This result assumes the neglect of viscosity and uses the approximation of the Lorentz force given by (3.23). This approximation is valid in the early stages of evolution. However, in the later stages, the vortex tubes are affected by viscous dissipation, leading to deviations in the structures of the magnetic and vortex tubes.

We investigate instances of initial magnetic tubes, following the methodology set forth by Xiong & Yang (2020a). Figure 8 illustrates the evolution of isosurfaces for $|\mathbf{b}|$ and $|\boldsymbol{\omega}|$ in the $L_m O_k$ case with $Re_m = 103.6$. As the magnetic field evolves, flux tubes undergo rapid topological changes, transitioning from quadrilateral to octagonal structures. The initial splitting of the tubes is accompanied by a notable release of magnetic energy and the formation of induced vortex tubes. These vortex tubes initially resemble magnetic tubes but decrease in intensity as kinetic energy dissipates, leading to outward diffusion of vorticity.

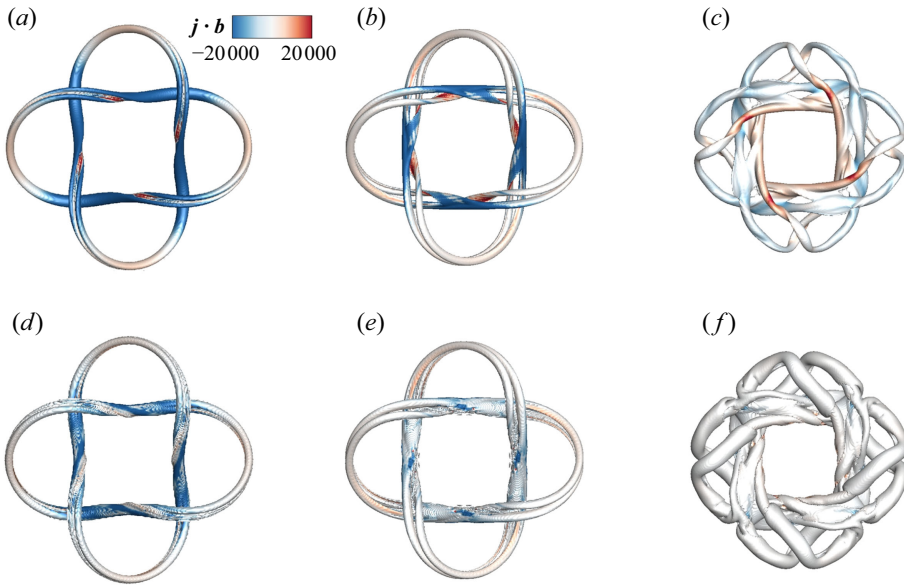


Figure 8. Isosurfaces of $|\mathbf{b}| = 50, 40$ and 20 (a–c) and $|\boldsymbol{\omega}| = 800, 800$ and 300 (d–f) for the $L_m O_k$ case with $Re_m = 1722.8$ at times (a,d) $t = 0.005$, (b,e) $t = 0.01$ and (c, f) $t = 0.05$. All isosurfaces are colour-coded by $\mathbf{j} \cdot \mathbf{b}$.

We further observe a phenomenon associated with the linkage of magnetic tubes, where the evolution of the isosurfaces $|\mathbf{b}|$ and $|\boldsymbol{\omega}|$ in the $L_m O_k$ configuration is identical to that observed in $R_m O_k$. In the initial stages of evolution, the fluid velocity is induced by the Lorentz force. This behaviour is examined through the velocity equation in (2.1), where the motion is governed by the magnetic field via the Lorentz force (2.2). Reversing the orientation of the magnetic tube from \mathbf{b} to $-\mathbf{b}$ does not affect \mathbf{F}_L or the induced velocity field. Consequently, the velocity fields in the $R_m O_k$ and $L_m O_k$ configurations are identical during the initial stage.

Taking the inner product of \mathbf{b} with the second equation in (2.1), we obtain the Lagrangian equation for the magnetic energy density:

$$\frac{D}{Dt} \frac{b^2}{2} = \mathcal{A}_m + \mathcal{B}_m, \tag{3.30}$$

where the right-hand-side components are defined as

$$\mathcal{A}_m = \alpha b^2 \quad \text{and} \quad \mathcal{B}_m = v_m \left(\frac{\nabla^2 b^2}{2} - \nabla \mathbf{b} : \nabla \mathbf{b} \right). \tag{3.31}$$

The first term, \mathcal{A}_m , represents the stretching effect, which is determined by the geometric evolution of the velocity field. The second term, \mathcal{B}_m , accounts for the dissipation of magnetic energy. Here, $\alpha = \mathbf{T} \cdot \nabla \mathbf{u} \cdot \mathbf{T}$ represents the stretching rate of an infinitely thin tube (Bajer & Moffatt 1997) and $\nabla \mathbf{b} : \nabla \mathbf{b}$ is the sum of the squares of each component of $\nabla \mathbf{b}$.

Equation (3.30) remains unchanged when \mathbf{b} is replaced with $-\mathbf{b}$, as both \mathcal{A}_m and \mathcal{B}_m are unaffected by the magnetic tube’s linkage. Thus, while the induced velocity interacts with the magnetic field, the linkage of the magnetic tube does not affect the evolution of magnetic strength. Additionally, as indicated by (3.11), it does not alter the magnitude

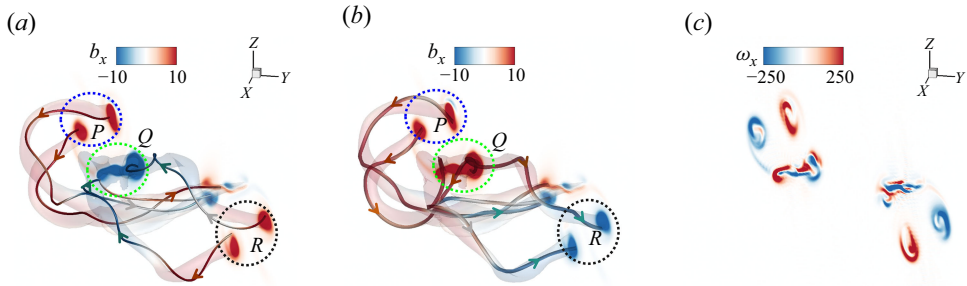


Figure 9. Magnetic and vorticity field comparison in the $L_m O_k$ and $R_m O_k$ cases. (a) Contour plots of b_x at $x = \pi$, along with semi-transparent isosurfaces of $|\mathbf{b}| = 20$ and integral trajectories of \mathbf{b} at $t = 0.05$ for the $L_m O_k$ case. (b) Same as (a) but for the $R_m O_k$ case. In both (a) and (b), the symbol P and symbols Q and R denote regions of identical and opposite b_x , respectively. (c) Contour plots of ω_x showing consistent patterns across both cases.

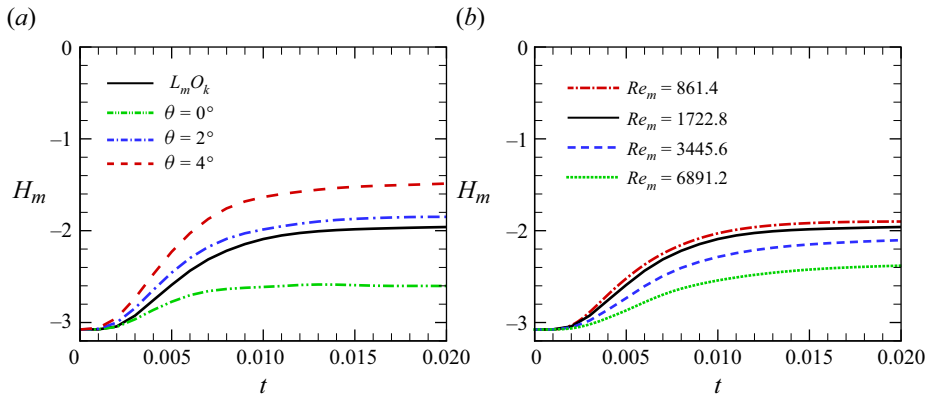


Figure 10. Temporal evolution of magnetic helicity H_m for (a) $L_m O_k$ and $L_m L_k$ with $Re_m = 103.6$, where different θ values represent varying angles between magnetic and vortex tubes for $L_m L_k$; (b) $L_m O_k$ with varying magnetic Reynolds numbers.

or direction of the Lorentz force. Consequently, the velocity–vorticity field in the fluid remains unchanged during the second stage.

Figure 9 compares the magnetic and vorticity fields in the $L_m O_k$ and $R_m O_k$ cases. Figures 9(a) and 9(b) display contour plots of b_x at $x = \pi$, along with semi-transparent isosurfaces of $|\mathbf{b}| = 20$ and integral trajectories of \mathbf{b} at $t = 0.05$ for each case. Although there are variations in the magnetic field in regions Q and R between figures 9(a) and 9(b), the vorticity fields remain consistent, as shown in figure 9(c). Additionally, as previously analysed, while linkage alters the direction of the magnetic field, it does not affect the geometry of the isosurfaces and magnetic field lines shown in figures 9(a) and 9(b).

3.4. The temporal evolution of helicity

Fluid statistics are influenced by the deformation of structural topology, as indicated by changes in helicity. Figure 10 presents the temporal evolution of magnetic helicity H_m for $L_m O_k$ at different magnetic Reynolds numbers and for $L_m L_k$ at various angles. Magnetic helicity initially increases rapidly before reaching a plateau, with the plateau value rising as the angle increases. This may be due to the reduced topological deformation when magnetic tubes and vortex tubes coincide. Additionally, the magnetic Reynolds number

also affects the extent of helicity changes. The mechanism driving the evolution of helicity is analysed in further detail.

We assume that the calculated helicity is a scalar field \mathcal{F} , defined as the dot product of the vectors \mathbf{G}_i and \mathbf{H}_j :

$$\mathcal{F} = \mathbf{G}_i \cdot \mathbf{H}_j, \tag{3.32}$$

where

$$\mathbf{G}_i = \nabla \times \mathbf{H}_i, \quad \nabla \cdot \mathbf{G}_i = 0 \quad (i = 1, 2). \tag{3.33}$$

Then,

$$\frac{\partial \mathcal{F}}{\partial t} = \frac{\partial \mathbf{G}_i}{\partial t} \cdot \mathbf{H}_j + (\nabla \times \mathbf{H}_i) \cdot \frac{\partial \mathbf{H}_j}{\partial t} = \nabla \cdot \left(\mathbf{H}_i \times \frac{\partial \mathbf{H}_j}{\partial t} \right) + \frac{\partial \mathbf{G}_j}{\partial t} \cdot \mathbf{H}_i + \frac{\partial \mathbf{G}_i}{\partial t} \cdot \mathbf{H}_j. \tag{3.34}$$

Here, \mathbf{G}_i can be the vorticity field $\boldsymbol{\omega}$ or the magnetic field \mathbf{b} . Their temporal evolution equations are

$$\frac{\partial \mathbf{G}_i}{\partial t} = \nabla \times (\mathbf{u} \times \mathbf{G}_i) + v_i \nabla^2 \mathbf{G}_i + \nabla \times \mathbf{F}_i. \tag{3.35}$$

When \mathbf{G}_i is the vorticity field, $\mathbf{F}_i = \mathbf{j} \times \mathbf{b}$; when \mathbf{G}_i is the magnetic field, $\mathbf{F}_i = \mathbf{0}$. Using the equation above, we have

$$\frac{\partial \mathbf{G}_i}{\partial t} \cdot \mathbf{H}_j = \nabla \times (\mathbf{u} \times \mathbf{G}_i) \cdot \mathbf{H}_j + v_i \nabla^2 \mathbf{G}_i \cdot \mathbf{H}_j + (\nabla \times \mathbf{F}_i) \cdot \mathbf{H}_j. \tag{3.36}$$

The three terms on the right-hand side of (3.36) can be rewritten as

$$\begin{cases} \nabla \times (\mathbf{u} \times \mathbf{G}_i) \cdot \mathbf{H}_j = \nabla \cdot (\mathbf{u} \times \mathbf{G}_i \times \mathbf{H}_j) + \mathbf{G}_j \cdot (\mathbf{u} \times \mathbf{G}_i), \\ \nabla^2 \mathbf{G}_i \cdot \mathbf{H}_j = \nabla \times (\nabla^2 \mathbf{H}_i) \cdot \mathbf{H}_j = \nabla \cdot (\nabla^2 \mathbf{H}_i \times \mathbf{H}_j) - \mathbf{G}_j \cdot (\nabla \times \mathbf{G}_i), \\ (\nabla \times \mathbf{F}_i) \cdot \mathbf{H}_j = \nabla \cdot (\mathbf{F}_i \times \mathbf{H}_j) + \mathbf{F}_i \cdot \mathbf{G}_j. \end{cases} \tag{3.37}$$

Substituting (3.37) into (3.36), we obtain

$$\frac{\partial \mathbf{G}_i}{\partial t} \cdot \mathbf{H}_j = \nabla \cdot \mathbf{W}_{ij} + \mathbf{G}_j \cdot (\mathbf{u} \times \mathbf{G}_i) - v_i \mathbf{G}_j \cdot (\nabla \times \mathbf{G}_i) + \mathbf{F}_i \cdot \mathbf{G}_j \tag{3.38}$$

with

$$\mathbf{W}_{ij} = \mathbf{u} \times \mathbf{G}_i \times \mathbf{H}_j + v_i \nabla^2 \mathbf{H}_i \times \mathbf{H}_j + \mathbf{F}_i \times \mathbf{H}_j. \tag{3.39}$$

According to the control volume transport formula for a fixed volume, the time rate of change of the integral of a scalar field \mathcal{F} over a fixed control volume Ω is given by

$$\frac{d}{dt} \int_{\Omega} \mathcal{F} dV = \int_{\Omega} \frac{\partial \mathcal{F}}{\partial t} dV + \int_{\partial \Omega} \mathcal{F} \mathbf{u} \cdot \mathbf{n} dS, \tag{3.40}$$

where \mathbf{n} is the outward unit normal to the stationary boundary $\partial \Omega$ and \mathbf{u} is the fluid velocity. By substituting (3.34) and (3.38) into (3.40), we obtain

$$\begin{aligned} \frac{d}{dt} \int_{\Omega} \mathcal{F} dV &= \int_{\partial \Omega} \mathbf{n} \cdot \left(\mathcal{F} \mathbf{u} + \mathbf{H}_i \times \frac{\partial \mathbf{H}_j}{\partial t} + \mathbf{W}_{ij} + \mathbf{W}_{ji} \right) dS \\ &+ \int_{\Omega} [-v_i \mathbf{G}_j \cdot (\nabla \times \mathbf{G}_i) - v_j \mathbf{G}_i \cdot (\nabla \times \mathbf{G}_j) + \mathbf{F}_i \cdot \mathbf{G}_j + \mathbf{F}_j \cdot \mathbf{G}_i] dV. \end{aligned} \tag{3.41}$$

For the numerical simulation conducted in a periodic cubic domain, the first term on the right-hand side of (3.41) vanishes due to the periodic boundary conditions. These conditions ensure that the flux across each face is exactly cancelled by the flux through the corresponding opposite face. Consequently, the net surface integral over $\partial\Omega$ reduces to zero.

The magnetic helicity is defined as $H_m = \int_{\Omega} \mathbf{a} \cdot \mathbf{b} \, dV$, where $\mathbf{b} = \nabla \times \mathbf{a}$. Using this definition, (3.41) simplifies to

$$\frac{dH_m}{dt} = -2\nu_m \int_{\Omega} b^2 (\nabla \times \mathbf{T}) \cdot \mathbf{T} \, dV, \tag{3.42}$$

where $\mathbf{b} = b\mathbf{T}$. At the initial moment, the first equation in (3.20) shows that $(\nabla \times \mathbf{T}) \cdot \mathbf{T} = 0$, indicating that the rate of change of H_m is zero. As time progresses, the magnetic field lines become chaotic. This change could be attributed to the Beltrami structure induced by the Beltrami field in the directions of \mathbf{N} and \mathbf{B} .

For the cross-helicity $H_c = \int_{\Omega} \mathbf{b} \cdot \mathbf{u} \, dV$, (3.41) can be simplified to

$$\frac{dH_c}{dt} = - \int_{\Omega} [v_k \mathbf{b} \cdot (\nabla \times \boldsymbol{\omega}) + \nu_m \boldsymbol{\omega} \cdot (\nabla \times \mathbf{b})] dV + \int_{\Omega} \mathbf{F}_L \cdot \mathbf{b} \, dV, \tag{3.43}$$

where $v_k = \nu_m$. Additionally, the term $\mathbf{b} \cdot (\nabla \times \boldsymbol{\omega}) + \boldsymbol{\omega} \cdot (\nabla \times \mathbf{b})$ can be rewritten as $\nabla \cdot (\boldsymbol{\omega} \times \mathbf{b}) + 2(\nabla \times \mathbf{b}) \cdot \boldsymbol{\omega}$, and $\mathbf{F}_L \cdot \mathbf{b} = 0$. Therefore, (3.43) can be further reduced to

$$\frac{dH_c}{dt} = -2\nu_m \left[\int_{\Omega} \boldsymbol{\omega} b (\nabla \times \mathbf{T}) \cdot \mathbf{T}_{\boldsymbol{\omega}} \, dV + \int_{\Omega} \boldsymbol{\omega} \nabla b \cdot (\mathbf{T} \times \mathbf{T}_{\boldsymbol{\omega}}) dV \right], \tag{3.44}$$

where $\boldsymbol{\omega} = \omega \mathbf{T}_{\boldsymbol{\omega}}$. This demonstrates the critical importance of the relative orientation of \mathbf{T} and $\mathbf{T}_{\boldsymbol{\omega}}$. When they are parallel, the second term becomes ineffective.

For the kinetic helicity $H_k = \int_{\Omega} \boldsymbol{\omega} \cdot \mathbf{u} \, dV$, (3.41) can be simplified to

$$\frac{dH_k}{dt} = -2\nu_k \int_{\Omega} \omega^2 \mathbf{T}_{\boldsymbol{\omega}} \cdot (\nabla \times \mathbf{T}_{\boldsymbol{\omega}}) dV + 2 \int_{\Omega} \boldsymbol{\omega} \mathbf{F}_L \cdot \mathbf{T}_{\boldsymbol{\omega}} \, dV. \tag{3.45}$$

The first term on the right-hand side represents the viscous dissipation of helicity. It involves the vorticity $\boldsymbol{\omega}$ and the unit vector $\mathbf{T}_{\boldsymbol{\omega}}$, which describe the geometry of vortex lines. This term indicates that viscous forces modify helicity by disrupting coherent vortex structures, with the dissipation rate proportional to the square of the vorticity magnitude $|\boldsymbol{\omega}|^2$. The second term represents the interaction between the vorticity field $\boldsymbol{\omega}$ and the Lorentz force \mathbf{F}_L . It accounts for the mechanical work done by electromagnetic forces on the fluid, which may either increase or decrease the kinetic helicity, depending on the relative alignment of the vorticity and force fields.

In the limit of infinite conductivity ($\sigma_m \rightarrow \infty$), where magnetic diffusivity $\nu_m = 0$ and the term $\nu_m \nabla^2 \mathbf{b}$ vanishes, the MHD equations reduce to their ideal form. In this regime, magnetic helicity is conserved, and the magnetic field topology remains unchanged. To observe changes in magnetic field topology in this study, we use higher resistivity settings.

Figure 11 illustrates the evolution of (3.42), (3.44) and (3.45) over time, compared with numerical differentiation results. This comparison validates the accuracy of both the theoretical derivation and the numerical simulation. With the chosen initial conditions, the rates of change for magnetic, cross and kinetic helicity are initially zero. When only magnetic tubes are present in the flow field, the rate of change of magnetic helicity increases significantly. The cross-helicity remains zero in the absence of vortex tubes due to the source term (3.44) being zero because of symmetry. When both magnetic and vortex tubes are present, the rates of change for both magnetic helicity and cross-helicity initially

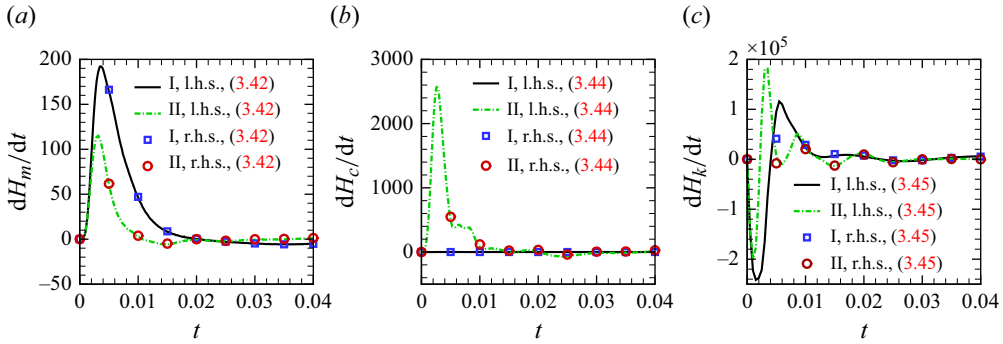


Figure 11. Numerical verification of the theoretical formulas: (a) equation (3.42), (b) equation (3.44) and (c) equation (3.45). The black solid and green dashed lines represent the left-hand-side terms, while the blue squares and red circles correspond to the right-hand-side terms for cases I, $L_m O_k$, and II, $L_m L_k$, with $\theta = 0^\circ$ and $Re_m = 861.4$.

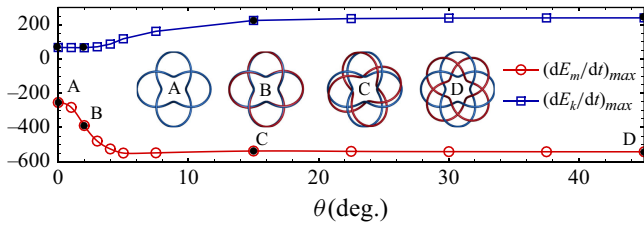


Figure 12. Maximum magnetic energy release rate $(dE_m/dt)_{max}$ and maximum kinetic energy increase rate $(dE_k/dt)_{max}$ as a function of the initial angle θ between the vortex tube and magnetic tube for the $L_m L_k$ cases with $Re_m = 103.6$. Insets A, B, C and D show isosurfaces of $|\mathbf{b}|$ (in blue) and $|\boldsymbol{\omega}|$ (in red) at $t = 0$ for $\theta = 0^\circ, 2^\circ, 15^\circ$ and 45° , respectively.

peak before rapidly dropping to zero, consistent with the rapid flattening observed in the helicity evolution discussed above (figure 10). Additionally, the rate of change of kinetic helicity initially drops rapidly to a negative value, then rises sharply to a positive value, before returning to near zero. The flow field exhibits vortex lines that twist, reconnect and break apart, eventually forming stable small-scale structures.

4. Vortex and magnetic tube interactions

4.1. Energy transfer in vortex and magnetic tube interactions

The angle between the structures is found to be highly sensitive, as illustrated by the evolution of helicity in figure 10. The effects of the relative orientation of the magnetic and vortex tubes on the dynamics is further investigated through the lens of energy and structural evolution. Figure 12 shows the variation in the maximum rate of magnetic energy release, $(dE_m/dt)_{max}$, and the maximum rate of kinetic energy increase, $(dE_k/dt)_{max}$, as functions of the initial angle θ between the magnetic and vortex tubes. A moderate Reynolds number of $Re_m = 103.6$ is considered in the $L_m L_k$ case. It is observed that $|(dE_m/dt)_{max}|$ increases rapidly with θ , reaching a peak at $\theta \approx 7.5^\circ$. In contrast, $(dE_k/dt)_{max}$ attains its maximum at $\theta = 0^\circ$ and decreases more rapidly as θ increases, with a minimum around $\theta = 5^\circ$. The most significant variations in these curves are observed at smaller values of θ , and thus the subsequent analysis is concentrated on this range.

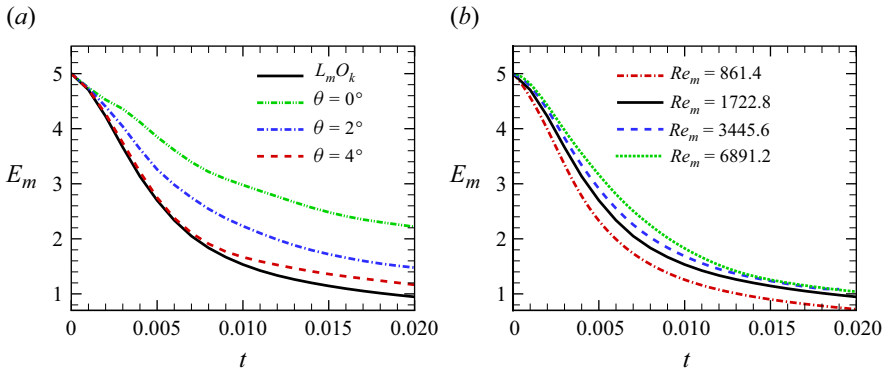


Figure 13. Temporal evolution of magnetic energy E_m for (a) $L_m O_k$ and $L_m L_k$ with $Re_m = 103.6$, where different θ values represent varying angles between magnetic and vortex tubes for $L_m L_k$; (b) $L_m O_k$ with varying magnetic Reynolds numbers.

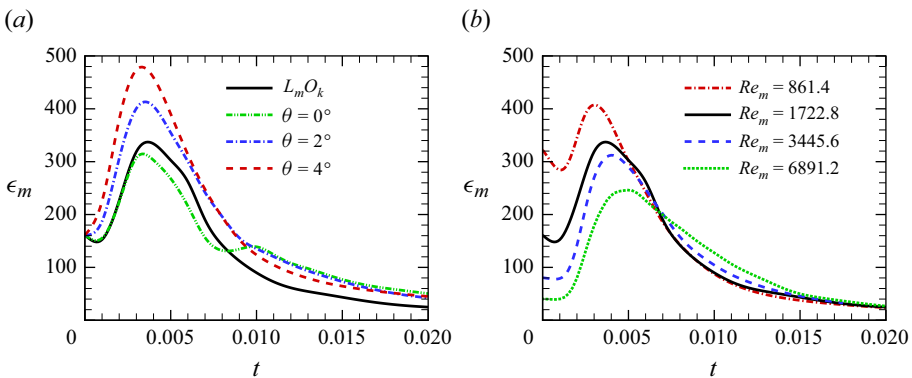


Figure 14. Temporal evolution of magnetic dissipation rate ϵ_m for (a) $L_m O_k$ and $L_m L_k$ with $Re_m = 103.6$, where different θ values represent varying angles between magnetic and vortex tubes for $L_m L_k$; (b) $L_m O_k$ with varying magnetic Reynolds numbers.

The maximum value of energy change is not the only factor showing notable angular sensitivity; the temporal evolution of energy also exhibits considerable variation. Figure 13 illustrates the temporal evolution of magnetic energy E_b under different conditions: $L_m L_k$, where the angles between magnetic and vortex tubes vary, and $L_m O_k$, involving different magnetic Reynolds numbers. Magnetic energy decreases over time due to resistive dissipation or conversion into kinetic energy. The presence of vortex tubes affects this evolution, resulting in a reduced release of magnetic energy compared with systems with only initial magnetic fields. The impact of vortex tubes on magnetic energy release is dependent on the angle between the tubes; even small changes, such as a 2° variation, can considerably alter the behaviour of the magnetic tube. Increasing the angle reduces mutual interaction, leading to more independent evolutions, while decreasing the angle enhances interaction, causing complex coupling effects that hinder magnetic energy release. Additionally, a reduction in magnetic viscosity slows the decay of magnetic energy, in line with expected viscous dissipation trends.

Magnetic energy changes can be assessed through the magnetic dissipation rates shown in figure 14, where all curves display an initial rise followed by a subsequent decline over time. Although figure 13 depicts a similar evolution of magnetic energy for $L_m O_k$ without

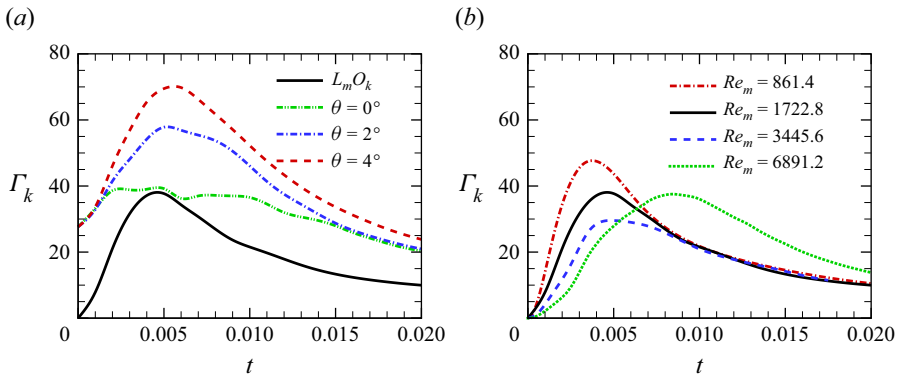


Figure 15. Temporal evolution of the kinetic dissipation rate ϵ_k for (a) $L_m O_k$ and $L_m L_k$ with $Re_m = 103.6$, where different θ values represent varying angles between magnetic and vortex tubes for $L_m L_k$; (b) $L_m O_k$ with varying magnetic Reynolds numbers.

an initial vortex tube and $L_m L_k$ with a 4° angle, figure 14 reveals differing dissipation rates between these scenarios. Specifically, the $L_m O_k$ case resembles the scenario with overlapping vortex and magnetic tubes more closely. This suggests that while overlapping vortex tubes do not markedly influence magnetic energy dissipation, they do reduce the conversion of magnetic energy into kinetic energy, leading to the slowest decrease in magnetic energy, as illustrated in figure 13. Moreover, in the later stages of evolution, the magnetic dissipation rate increases for configurations with overlapping magnetic and vortex tubes, contrasting with cases involving only magnetic tubes. This discrepancy is attributed to geometric and topological changes in the structure of the two cases during the later stages. Specifically, magnetic tubes undergo splitting during free evolution, whereas in the presence of vortex tube constraints, they do not. This results in behaviour that diverges from that of the initial phase.

The interaction between vortex and magnetic tubes has a substantial effect on the conversion of magnetic energy to kinetic energy and its subsequent dissipation. Overlapping vortex and magnetic tubes restrict the conversion of magnetic energy, leading to reduced peaks in kinetic energy dissipation, as illustrated in figure 15. In contrast, other configurations display more pronounced dissipation peaks. These peaks are associated with structural splitting in the flow, involving extensive topological reconnections and disconnections. Additionally, an increase in the Reynolds number delays both the dissipation peaks and the topological changes in the magnetic tubes, as shown in figure 15(b).

We investigate the morphological evolution of flux tubes across four angles, $\theta = 0^\circ$, 2° , 15° and 45° , as depicted in figure 16. This examination reveals the development of isosurfaces $|\mathbf{b}|$, colour-coded by $\mathbf{b} \cdot \mathbf{u}$, and isosurfaces $|\boldsymbol{\omega}|$ in light grey, captured at $t = 0.05$. The angle θ influences the morphological changes in magnetic tubes.

At small angles, such as $\theta = 0^\circ$ and 2° , the vortex tube inhibits the splitting of the magnetic tube. While the magnetic tube initially undergoes partial splitting, this process is suppressed by the presence of the vortex tube. The vortex tube's morphology remains largely unchanged, whereas the magnetic tube adapts to its evolution. We investigate the evolution of vortex tubes with different linkages undergoing free decay in viscous flows. Left-handed linkages elongate, interact strongly and dissipate viscously, generating vorticity gradients that drive reconnection and scale cascade processes. In contrast, right-handed linkages exhibit collective rotation, reconnection and disconnection, evolving into

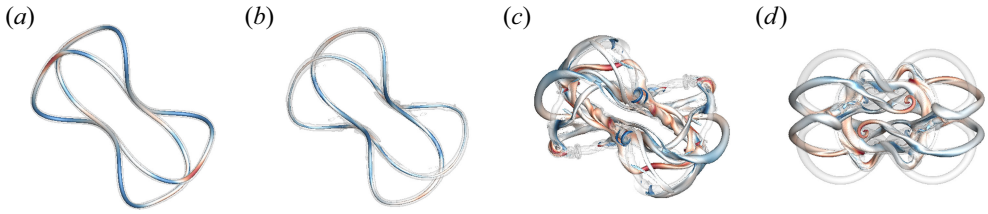


Figure 16. Isosurfaces of $|\mathbf{b}| = 100$ and $|\boldsymbol{\omega}| = 300$ for the $L_m L_k$ cases with $Re_m = 103.6$ at $t = 0.05$ for (a) $\theta = 0^\circ$, (b) $\theta = 2^\circ$, (c) $\theta = 15^\circ$ and (d) $\theta = 45^\circ$. Magnetic tubes are rendered based on $\mathbf{b} \cdot \mathbf{u}$, with vortex tubes shown in light grey. Vortex tubes may be obscured by magnetic tubes at smaller angles but are visible separately at larger angles.

large-scale, unknotted vortex rings rather than small-scale structures that transition rapidly to turbulence (see Xiong & Yang 2019a). In MHD flows with a non-trivial magnetic field, these effects further influence the late-stage evolution of magnetic flux tubes through nonlinear coupling. Conversely, at larger angles like $\theta = 45^\circ$, the vortex tube does not obstruct the initial splitting of the magnetic tube for $t < 0.01$, leading to a rapid release of magnetic energy. However, it alters the structure of the magnetic tube, as evidenced by considerable transverse stretching at $\theta = 45^\circ$. Additionally, after $t > 0.05$, as the vorticity field weakens, its effect on the interaction between the vortex and magnetic tubes diminishes.

4.2. Annihilation of vortex dipoles

Based on the preceding analysis, we find that the Lorentz force generated by a magnetic tube induces the formation of counter-rotating vortices, leading to a self-splitting effect. Furthermore, the presence of initial vortex tubes can affect the evolution of magnetic tubes, especially when the initial vortex is aligned with the magnetic tube. In these instances, the magnetic tubes show minimal splitting, and their morphology evolves closely in alignment with that of the vortex tubes.

Figure 17 illustrates the flow field around magnetic flux tubes for the $L_m O_k$ and $L_m L_k$ cases, as shown by the streamlines. In the $L_m O_k$ set-up, vortex dipoles and tube splitting are observed. In contrast, in the $L_m L_k$ case, where the vortex tube is aligned with the magnetic tube, vortex dipole formation is suppressed, preventing splitting. This finding aligns with the mechanism described by Xiong & Yang (2020a), which posits that magnetic field line torsion inhibits magnetic tube splitting. In both scenarios, the local distribution of vortices is adjusted to reduce vortex dipole formation.

Figure 18(a) presents plane cuts of the contour for $F_{L,y} = \mathbf{e}_y \cdot \mathbf{F}_L$ at $t = 0$ and $z = 1.63$, which corresponds to the magnetic tube's symmetry plane in the z direction. The contour shows positive values of $F_{L,y}$ in the upper part of the tube and negative values in the lower part. Likewise, $F_{L,x}$ (which is $\mathbf{e}_x \cdot \mathbf{F}_L$) is positive on the right-hand side of the tube and negative on the left-hand side (not shown). The streamline in figure 18(a) represents the projection of the Lorentz force onto the plane, extending outward from the centre, and contributes to the tube's expansion and splitting. Figures 18(b) and 18(c) depict the projections of velocity streamlines and contours of $F_{L,y}$ at $t = 0.005$ for the $L_m O_k$ and $L_m L_k$ scenarios, as shown in figure 17. In the absence of the vortex tube, the magnetic tube undergoes splitting, resulting in a dipole-like velocity field. Conversely, when the initial vortex tube is present, the Lorentz force continues to drive the magnetic tube towards splitting; however, the tube remains intact. Consequently, the velocity field around the magnetic tube exhibits a point vortex configuration.

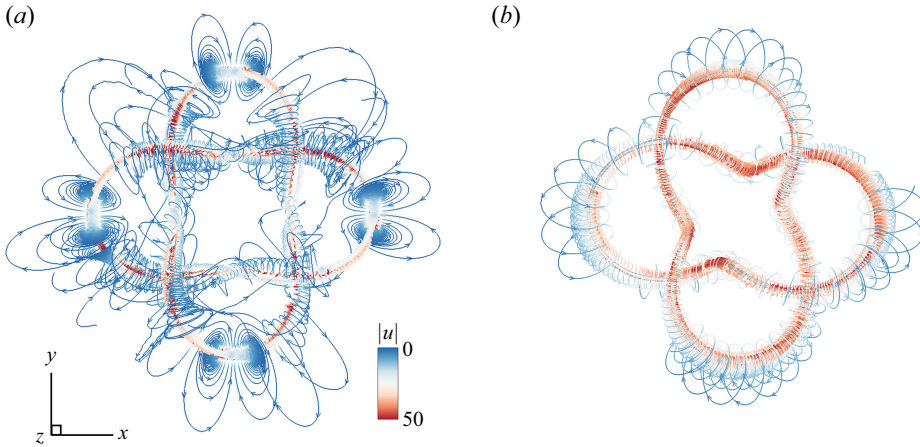


Figure 17. Streamlines colour-coded by the magnitude of $|\mathbf{u}|$ for two cases with $Re_m = 103.6$: (a) $L_m O_k$ and (b) $L_m L_k$ with $\theta = 0$ at $t = 0.005$.

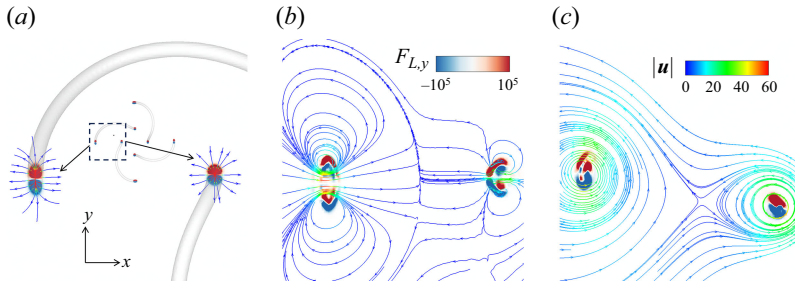


Figure 18. Velocity field and Lorentz force for MHD flows with $Re_m = 103.6$ within the dashed box in (a), with the isocontour at $z = 1.63$ showing $F_{L,y} = \mathbf{e}_y \cdot \mathbf{F}_L$. The lines in (a) represent the projection of the vector field \mathbf{F}_L onto the plane at $z = 1.63$ at the initial stage for the $L_m O_k$ case. The lines in (b) and (c) represent the projection of the velocity field \mathbf{u} onto the plane at $z = 1.63$ at $t = 0.005$ for the $L_m O_k$ and $L_m L_k$ cases, respectively. The colourbar for $F_{L,y}$ applies to (a–c), while the colourbar for $|\mathbf{u}|$ applies to (b,c).

Based on (3.30) and (3.31), we analyse the influence of energy transfer on MHD flow dynamics. Figure 19 illustrates the temporal evolution of the stretching term \mathcal{A}_m and the dissipative term \mathcal{B}_m across various configurations: pure magnetic tubes ($R_m O_k$ and $L_m O_k$) and configurations with aligned magnetic and vortex tubes ($R_m R_k$ and $L_m L_k$). For pure magnetic tubes, \mathcal{A}_m and \mathcal{B}_m initially exhibit no dependence on linkage, with notable changes occurring around $t = 0.005$ and a gradual decrease beyond $t > 0.02$. Negative values of \mathcal{A}_m are associated with tube splitting, which facilitates the conversion of magnetic energy into kinetic energy. In contrast, for the aligned configurations, particularly $L_m L_k$, \mathcal{A}_m is positive, indicating an energy transfer from the vortex to the magnetic tube. While the influence of the dissipative term is relatively minor in both scenarios, its effect is prolonged when both magnetic and vortex tubes are present compared with cases involving only magnetic tubes.

We present the magnitudes of the vorticity fields induced by both the magnetic tube and the additional vortex tube. This analysis reveals that an additional vortex tube with strength comparable to that of the magnetic tubes can prevent the formation of vortex dipoles, thereby inhibiting magnetic tube splitting. For the magnetic tube described by the initial condition in (2.3), we take $R_v = 5\sigma \approx 0.125$ as the characteristic length.

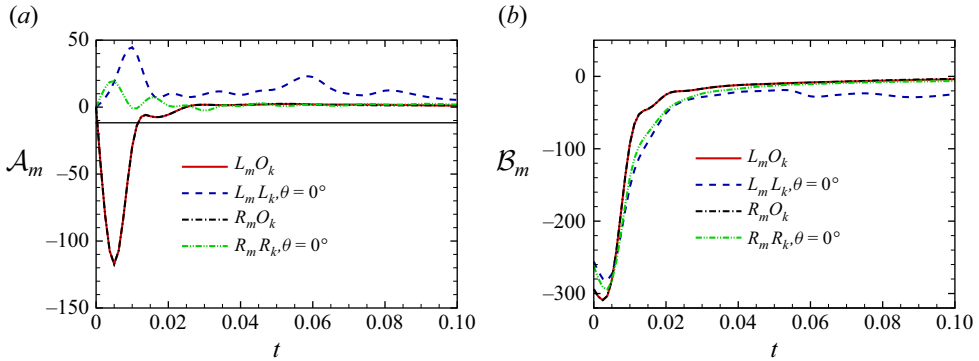


Figure 19. Temporal evolution of (a) $\mathcal{A}_m = \alpha b^2$ and (b) $\mathcal{B}_m = \nu_m(\nabla^2 b^2/2 - \nabla \mathbf{b} : \nabla \mathbf{b})$ in the DNS of MHD flows with $Re_m = 103.6$.

The characteristic magnitude of \mathbf{b} is given by the maximum value $b_{max} = \Gamma_m/(2\pi\sigma^2) \approx 265$, measured at $\varrho = 0$. The characteristic time interval for rapid magnetic energy release is set to $T_c = 0.005$, as indicated in figures 13 and 14.

In the $L_m O_k$ case, the linearised vorticity equation at the initial time is given by

$$\frac{\partial \omega}{\partial t} - \nu \nabla^2 \omega = \nabla \times \mathbf{F}_L. \tag{4.1}$$

The magnitude of $\nabla \times \mathbf{F}_L$ can be estimated using (3.21) as $O(|\nabla \times \mathbf{F}_L|) \sim O(|\mathbf{B} \cdot \nabla(b^2\kappa)|) \approx \max(b^2\kappa)/R_v \approx 8.4 \times 10^5$. Consequently, the magnitude of vorticity induced by the magnetic tube is approximately $T_c \cdot O(|\nabla \times \mathbf{F}_L|) \approx 4.2 \times 10^3$. Thus, the initial magnetic tubes generate dipole vortex tubes with a magnitude of 4.2×10^3 and opposite directions. For an initial vortex tube of the form $\omega_r = \Gamma_k/(2\pi\sigma^2) \exp[-r^2/(2\sigma^2)]$, the vorticity magnitude is also approximately $\Gamma_k/(2\pi\sigma^2) \approx 4.4 \times 10^3$. Therefore, introducing a vortex tube aligned with the initial magnetic tube enhances the vorticity of the same sign while diminishing the vorticity of the opposite sign, thereby inhibiting splitting.

5. Conclusion

We analyse MHD flows using DNS, concentrating on the interaction between magnetic and vortical flux tubes. Our study elucidates how the linkages and angles between these tubes influence the release, dissipation and conversion of magnetic and kinetic energies. We emphasise the critical impact of geometric factors on the system’s evolution.

In the absence of an initial magnetic field, vortices with different linkages exhibit distinct behaviours: left-handed linkage vortices experience considerable viscous dissipation and fragmentation at smaller scales, while right-handed linkage vortices exhibit collective rotational motion, forming larger, cohesive structures. Without initial vorticity, both magnetic and induced vorticity fields evolve consistently, displaying quasi-Lagrangian material properties (see figure 8). The rapid changes in helicity occur only in the early stages of evolution (see figure 11), during which magnetic flux tubes generate dipole vortices via Lorentz forces (see figure 18), leading to the splitting of magnetic tubes into finer structures. This process involves conversion and release of magnetic energy, influenced by the curvature geometry of the magnetic tubes (see figure 6).

The presence of vortex tubes can hinder the formation of induced vortex dipoles within magnetic tubes, thereby preventing their splitting (see figure 17). Furthermore, even small misalignments of $1^\circ - 2^\circ$ between vortex and magnetic tubes can result in markedly

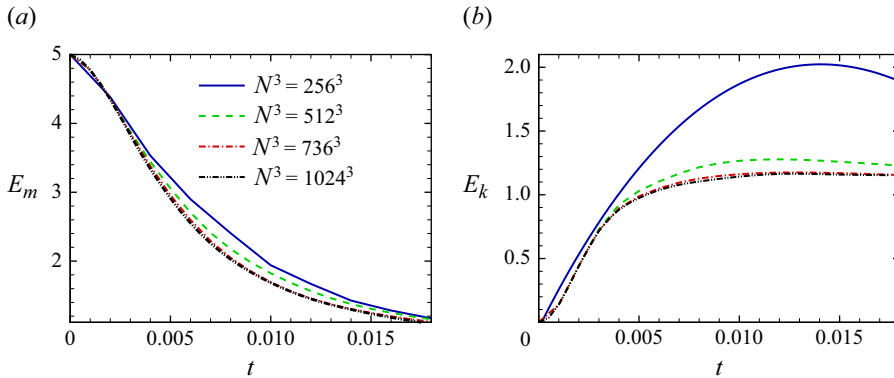


Figure 20. Temporal evolution of (a) magnetic energy E_m and (b) kinetic energy E_k for the $L_m O_k$ case with the minimum v_m from the examples calculated in this study at various grid resolutions. The legend in (b) is omitted as it duplicates that in (a).

different energy release mechanisms (see figure 12). The strongest interactions occur when magnetic and vortex tubes coincide; in such cases, vortex tubes inhibit both the topological splitting and energy release of the magnetic tubes. These results align with earlier experimental observations by Spruit & Roberts (1983).

We also introduce the FS frame field analysis method in § 3.1, which allows for a streamlined expression of the Lorentz force (see (3.11)) and its curl field (see (3.13)). This approach enables a detailed quantitative analysis of magnetic tube splitting mechanisms and isolates the primary mechanism of induced splitting, namely the alignment of the curl of Lorentz force with the tangent direction of the magnetic field lines, which is related to the curvature of these lines. This method can be extended as a general vector field analysis technique, especially in cases where field helicity is dependent solely on writhe, providing a concise formulation of frame divergence and curl (see (3.19) and (3.20)).

Future research may focus on examining additional parameters, such as varying viscosities or magnetic diffusivities, to gain a deeper understanding of the interplay between dissipation and energy transfer in MHD flows. Exploring different initial configurations and spatial scales could provide further insights into the dynamics of magnetic and vortical structures. Additionally, investigating the effects of external perturbations or constraints on flux tube behaviour may offer new strategies for controlling or manipulating these flows, with potential applications in engineering and astrophysics. Integrating experimental data with computational simulations could also enhance our understanding of these complex fluid dynamics systems.

Acknowledgements. The authors acknowledge support from the National Natural Science Foundation of China (grant nos. 12302294, 12102365 and 12432010).

Declaration of interests. The authors report no conflict of interest.

Appendix A. Grid convergence analysis

Previous studies have demonstrated that a 512^3 grid resolution is sufficient to obtain accurate results under moderate conditions, as shown in Hao *et al.* (2019). To evaluate the numerical accuracy of our simulations under more extreme conditions, we conduct a grid convergence study of the magnetic and kinetic energy for the $L_m O_k$ case with the minimum v_m from the examples calculated in this study. A DNS is performed on grids with resolutions of 256^3 , 512^3 , 768^3 and 1024^3 . As shown in figure 20, the energy

profiles converge at the 1024^3 grid resolution, confirming that the grid resolution used in our simulations, as specified in table 1, is adequate.

REFERENCES

- ALFVÉN, H. 1943 On the existence of electromagnetic-hyromagnetic waves. *Ark. Mat. Astron. Fys.* **29**, 1–7.
- ALUIE, H. 2009 *Hydrodynamic and Magnetohydrodynamic Turbulence: Invariants, Cascades, and Locality*. The Johns Hopkins University.
- ANGELOPOULOS, V., ARTEMYEV, A., PHAN, T.D. & MIYASHITA, Y. 2020 Near-earth magnetotail reconnection powers space storms. *Nat. Phys.* **16** (3), 317–321.
- BAJER, K. & MOFFATT, H.K. 1997 On the effect of a central vortex on a stretched magnetic flux tube. *J. Fluid Mech.* **339**, 121–142.
- BECKERS, J.M. & SCHRÖTER, E.H. 1968 The intensity, velocity and magnetic structure of a sunspot region. *Solar Phys.* **4** (2), 142–164.
- BERCIU, M., RAPPOPORT, T.G. & JANKÓ, B. 2005 Manipulating spin and charge in magnetic semiconductors using superconducting vortices. *Nature* **435** (7038), 71–75.
- BISKAMP, D. 1994 Magnetic reconnection. *Phys. Rep.* **237** (4), 179–247.
- BOWERS, C.F., SLAVIN, J.A., DIBRACCIO, G.A., POH, G., HARA, T., XU, S. & BRAIN, D.A. 2021 Maven survey of magnetic flux rope properties in the martian ionosphere: comparison with three types of formation mechanisms. *Geophys. Res. Lett.* **48** (10), e2021GL093296.
- CASSAK, P.A., SHAY, M.A. & DRAKE, J.F. 2005 Catastrophe model for fast magnetic reconnection onset. *Phys. Rev. Lett.* **95** (23), 235002.
- CHELPANOV, A.A., KOBANOV, N.I. & KOLOBOV, D.Y. 2015 Characteristics of oscillations in magnetic knots of solar faculae. *Astron. Rep.* **59** (10), 968–973.
- DAVIDSON, P.A. 2017 *Introduction to Magnetohydrodynamics*, Cambridge Texts in Applied Mathematics, vol. 55. Cambridge University Press.
- DOMÍNGUEZ-LOZOYA, J.C., CUEVAS, S., DOMÍNGUEZ, D.R., Á. VALOS-ZÚ NIGA, R. & RAMOS, E. 2021 Laboratory characterization of a liquid metal mhd generator for ocean wave energy conversion. *Sustainability* **13** (9), 4641.
- DUMIN, Y.V. & SOMOV, B.V. 2019 Topological model of the anemone microflares in the solar chromosphere. *Astron. Astrophys.* **623**, L4.
- DUMIN, Y.V. & SOMOV, B.V. 2020 New types of the chromospheric anemone microflares: case study. *Solar Phys.* **295** (7), 1–10.
- EFFENBERG, F., FENG, Y., SCHMITZ, O., FRERICHS, H., BOZHENKOV, S.A., HÖLBE, H., KÖNIG, R., KRYCHOWIAK, M., PEDERSEN, T.S. & REITER, D. 2017 Numerical investigation of plasma edge transport and limiter heat fluxes in Wendelstein 7-X startup plasmas with EMC3-EIRENE. *Nucl. Fusion* **57** (3), 036021.
- EGEDAL, J., LE, A. & DAUGHTON, W. 2013 A review of pressure anisotropy caused by electron trapping in collisionless plasma, and its implications for magnetic reconnection. *Phys. Plasmas* **20** (6), 061201.
- ELSASSER, W.M. 1950 The hydromagnetic equations. *Phys. Rev.* **79** (1), 183–183.
- FAN, Y. 2008 The three-dimensional evolution of buoyant magnetic flux tubes in a model solar convective envelope. *Astrophys. J.* **676** (1), 680–697.
- FREIDBERG, J.P., MANGIAROTTI, F.J. & MINERVINI, J. 2015 Designing a tokamak fusion reactor—how does plasma physics fit in? *Phys. Plasmas* **22** (7), 070901.
- GIBBON, J.D., HOLM, D.D., KERR, R.M. & ROULSTONE, I. 2006 Quaternions and particle dynamics in the Euler fluid equations. *Nonlinearity* **19** (8), 1969–1983.
- GONZALEZ, W.D., JOSELYN, J.A., KAMIDE, Y., KROEHL, H.W., ROSTOKER, G., TSURUTANI, B.T. & VASYLIUNAS, V.M. 1994 What is a geomagnetic storm? *J. Geophys. Res. Space Phys.* **99** (A4), 5771–5792.
- GOOSSENS, M., RUDERMAN, M.S. & HOLLWEG, J.V. 1995 Dissipative MHD solutions for resonant Alfvén waves in 1-dimensional magnetic flux tubes. *Solar Phys.* **157** (1–2), 75–102.
- HAO, J., XIONG, S. & YANG, Y. 2019 Tracking vortex surfaces frozen in the virtual velocity in non-ideal flows. *J. Fluid Mech.* **863**, 513–544.
- HAO, J. & YANG, Y. 2021 Magnetic knot cascade via the stepwise reconnection of helical flux tubes. *J. Fluid Mech.* **912**, A48.
- HASIMOTO, H. 1959 Magnetohydrodynamic wave of finite amplitude at magnetic Prandtl number 1. *Phys. Fluids* **2** (5), 575–576.

- HELMHOLTZ, H. 1858 Über integrale der hydrodynamischen gleichungen, welche den wirbelbewegungen entsprechen. *J. Reine Angew. Math.* **55**, 25–55.
- HOELZL, M., HUIJMANS, G.T.A., PAMELA, S.J.P., BÉCOULET, M., NARDON, E., ARTOLA, F.J., NKONGA, B., ATANASIU, C.V., BANDARU, V. & BHOLE, A. 2021 The JOREK non-linear extended MHD code and applications to large-scale instabilities and their control in magnetically confined fusion plasmas. *Nucl. Fusion* **61** (6), 065001.
- INOUE, S., KUSANO, K., BÜCHNER, J. & SKÁLA, J. 2018 Formation and dynamics of a solar eruptive flux tube. *Nat. Commun.* **9** (1), 174.
- JI, H., DAUGHTON, W., JARA-ALMONTE, J., LE, A., STANIER, A. & YOO, J. 2022 Magnetic reconnection in the era of exascale computing and multiscale experiments. *Nat. Rev. Phys.* **4** (4), 263–282.
- KIVOTIDES, D. 2018 Interactions between vortex tubes and magnetic-flux rings at high kinetic and magnetic Reynolds numbers. *Phys. Rev. Fluids* **3** (3), 033701.
- KIVOTIDES, D. 2019 Interactions between vortex and magnetic rings at high kinetic and magnetic Reynolds numbers. *Phys. Lett. A* **383** (14), 1601–1606.
- KULSRUD, R.M. 1983 MHD description of plasma. In *Handbook of Plasma Physics*, vol. 1, pp. 115. North-Holland.
- LAZARIAN, A. & VISHNIAC, E.T. 1999 Reconnection in a weakly stochastic field. *Astrophys. J.* **517** (2), 700–718.
- LEVCHENKO, I., XU, S., MAZOUFFRE, S., LEV, D., PEDRINI, D., GOEBEL, D., GARRIGUES, L., TACCOGNA, F. & BAZAKA, K. 2020 Perspectives, frontiers, and new horizons for plasma-based space electric propulsion. *Phys. Plasmas* **27** (2), 020601.
- LINTON, M.G., DAHLBURG, R.B. & ANTIOCHOS, S.K. 2001 Reconnection of twisted flux tubes as a function of contact angle. *Astrophys. J.* **553** (2), 905–921.
- LOZITSKY, V.G., BARANOVSKY, E.A., LOZITSKA, N.I. & LEIKO, U.M. 2000 Observations of magnetic field evolution in a solar flare. *Astron. Rep.* **191**, 171–183.
- LUNDGREN, T.S. 1982 Strained spiral vortex model for turbulent fine structure. *Phys. Fluids* **25** (12), 2193–2203.
- LUNDGREN, T.S. 1993 A small-scale turbulence model. *Phys. Fluids A* **5** (6), 1472–1483.
- MACTAGGART, D., PRIOR, C., RAPHALDINI, B., ROMANO, P. & GUGLIELMINO, S.L. 2021 Direct evidence that twisted flux tube emergence creates solar active regions. *Nat. Commun.* **12** (1), 6621.
- MAKWANA, K.D. & YAN, H. 2020 Properties of magnetohydrodynamic modes in compressively driven plasma turbulence. *Phys. Rev. X* **10** (3), 031021.
- MANEK, B. & BRUMMELL, N. 2021 On the origin of solar hemispherical helicity rules: simulations of the rise of magnetic flux concentrations in a background field. *Astrophys. J.* **909** (1), 72.
- MININNI, P.D., POUQUET, A.G. & MONTGOMERY, D.C. 2006 Small-scale structures in three-dimensional magnetohydrodynamic turbulence. *Phys. Rev. Lett.* **97** (24), 244503.
- ÖZDEMİR, Z. 2021 A geometrical and physical interpretation of quaternionic generalized magnetic flux tubes. *Chaos, Solitons Fractals* **143**, 110541.
- PARKER, E.N. 1978 The mutual attraction of magnetic knots. *astrophys. Astrophys. J.* **222**, 357–364.
- PORTO, J., ELIAS, P.Q. & CIARDI, A. 2023 Anisotropic electron heating in an electron cyclotron resonance thruster with magnetic nozzle. *Phys. Plasmas* **30** (2), 023506.
- PRIEST, E. & FORBES, T. 2000 *Magnetic Reconnection: MHD Theory and Applications*. Cambridge University Press.
- REED, D. 1995 Foundational electrodynamics and Beltrami vector fields. In *Advanced Electromagnetism: Foundations, Theory and Applications*, pp. 217–249. World Scientific Publishing.
- REN, Y., YAMADA, M., GERHARDT, S., JI, H., KULSRUD, R. & KURITSYN, A. 2005 Experimental verification of the Hall effect during magnetic reconnection in a laboratory plasma. *Phys. Rev. Lett.* **95** (5), 055003.
- RICCA, R.L. 1997 Evolution and inflexional instability of twisted magnetic flux tubes. *Solar Phys.* **172** (1/2), 241–248.
- RICCA, R.L. 2005 Inflexional disequilibrium of magnetic flux-tubes. *Fluid Dyn. Res.* **36** (4–6), 319–332.
- RICCA, R.L. 2013 New energy and helicity bounds for knotted and braided magnetic fields. *Geophys. Astrophys. Fluid Dyn.* **107** (4), 385–402.
- RICCA, R.L. & MAGGIONI, F. 2014 On the groundstate energy spectrum of magnetic knots and links. *J. Phys. A Math. Theor.* **47** (20), 205501.
- ROBERTS, B. & WEBB, A.R. 1978 Vertical motions in an intense magnetic flux tube. *Solar Phys* **56** (1), 5–35.
- SINGH, N., DEVERAPALLI, C. & KHAZANOV, G. 2006 Electrodynamics in a very thin current sheet leading to magnetic reconnection. *Nonlinear Process. Geophys.* **13** (5), 509–523.

- SMIET, C.B., CANDELARESI, S., THOMPSON, A., SWEARINGIN, J., DALHUISEN, J.W. & BOUWMEESTER, D. 2015 Self-organizing knotted magnetic structures in plasma. *Phys. Rev. Lett.* **115** (9), 095001.
- SOMOV, B.V. & KOSUGI, T. 1997 Collisionless reconnection and high-energy particle acceleration in solar flares. *Astrophys. J.* **485** (2), 859–868.
- SPICER, D.S. 1982 Magnetic energy storage and conversion in the solar atmosphere. *Space Sci. Rev.* **31** (4), 351–435.
- SPRUIT, H.C. & ROBERTS, B. 1983 Magnetic flux tubes on the sun. *Nature* **304** (5925), 401–406.
- STUIKYS, A. & SYKULSKI, J. 2018 Rapid multi-objective design optimisation of switched reluctance motors exploiting magnetic flux tubes. *IET Sci. Meas. Technol.* **12** (2), 223–229.
- TANG, J., DING, X., ZHANG, P., LEI, B., ZHAO, Z. & DUAN, Y. 2018 A highly efficient magnetically confined ion source for real time on-line monitoring of trace compounds in ambient air. *Chem. Commun.* **54** (92), 12962–12965.
- TAO, R., REN, H., TONG, Y. & XIONG, S. 2021 Construction and evolution of knotted vortex tubes in incompressible Schrödinger flow. *Phys. Fluids* **33** (7), 077112.
- TORIUMI, S. & HOTTA, H. 2019 Spontaneous generation of δ -sunspots in convective magnetohydrodynamic simulation of magnetic flux emergence. *Astrophys. J. Lett.* **886**, L21.
- TZIOTZIOU, K., *et al.* 2023 Vortex motions in the solar atmosphere: definitions, theory, observations, and modelling. *Space Sci. Rev.* **219** (1), 1.
- XIONG, S., WANG, Z., WANG, M. & ZHU, B. 2022 A Clebsch method for free-surface vortical flow simulation. *ACM Trans. Graph.* **41** (4), 116–13.
- XIONG, S. & YANG, Y. 2019a Construction of knotted vortex tubes with the writhe-dependent helicity. *Phys. Fluids* **31** (4), 047101.
- XIONG, S. & YANG, Y. 2019b Identifying the tangle of vortex tubes in homogeneous isotropic turbulence. *J. Fluid Mech.* **874**, 952–978.
- XIONG, S. & YANG, Y. 2020a Effects of twist on the evolution of knotted magnetic flux tubes. *J. Fluid Mech.* **895**, A28.
- XIONG, S. & YANG, Y. 2020b Evolution and helicity analysis of linked vortex tubes in viscous flows. *Sci. Sin. Phys. Mech. Astron.* **50** (4), 040005.
- YAMADA, M., KULSRUD, R. & JI, H. 2010 Magnetic reconnection. *Rev. Mod. Phys.* **82** (1), 603–664.
- YANG, S., XIONG, S., ZHANG, Y., FENG, F., LIU, J. & ZHU, B. 2021 Clebsch gauge fluid. *ACM Trans. Graph.* **40**, 99.
- YIN, L., DAUGHTON, W., KARIMABADI, H., ALBRIGHT, B.J., BOWERS, K.J. & MARGULIES, J. 2008 Three-dimensional dynamics of collisionless magnetic reconnection in large-scale pair plasmas. *Phys. Rev. Lett.* **101** (12), 125001.
- YOU, S., YUN, G.S. & BELLAN, P.M. 2005 Dynamic and stagnating plasma flow leading to magnetic-flux-tube collimation. *Phys. Rev. Lett.* **95** (4), 045002.
- YUAN, Y., SPITKOVSKY, A., BLANDFORD, R.D. & WILKINS, D.R. 2019 Black hole magnetosphere with small-scale flux tubes – II. Stability and dynamics. *Mon. Not. R. Astron. Soc.* **487** (3), 4114–4127.
- ZHAO, X. & SCALO, C. 2021 Helicity dynamics in reconnection events of topologically complex vortex flows. *J. Fluid Mech.* **920**, A30.
- ZHUGZHDA, Y.D. 2000 Nonlinear waves in thin magnetic flux tubes in astrophysical plasma. *Phys. Scr.* **T84** (1), 159–162.
- ZWEIBEL, E.G. & YAMADA, M. 2009 Magnetic reconnection in astrophysical and laboratory plasmas. *Annu. Rev. Astron. Astrophys.* **47** (1), 291–332.